FULLY NON-CONTACT, AIR-COUPLED GENERATION AND DETECTION OF ULTRASOUND IN CONCRETE FOR NONDESTRUCTIVE TESTING

A Thesis
Presented to
The Academic Faculty

by

Fabian Schempp

In Partial Fulfillment
of the Requirements for the Degree
Master of Science in Engineering Science and Mechanics in the
School of Civil and Environmental Engineering

Georgia Institute of Technology
December 2013

FULLY NON-CONTACT, AIR-COUPLED GENERATION AND DETECTION OF ULTRASOUND IN CONCRETE FOR NONDESTRUCTIVE TESTING

Approved by:

Dr. Laurence Jacobs, Advisor
School of Civil and Environmental Engineering
Georgia Institute of Technology

Dr. Jin-Yeon Kim
School of Civil and Environmental Engineering
Georgia Institute of Technology

Dr. Reginald DesRoches
School of Civil and Environmental Engineering
Georgia Institute of Technology

Date Approved: 18 November 2013

ACKNOWLEDGEMENTS

First of all I want to thank everyone who made this program and my stay in the United States possible. Primarily, I want to express me sincerest gratitude to Dr. Laurence J. Jacobs whose incredible commitment to this program made it possible for many young people over the last 15 years to come to Atlanta and study in the United Stated at one of the best engineering schools in the country. His academic and also administrative support and his motivation made this thesis possible. Dr. Jacobs gave me also the opportunity to present my results at the QNDE conference in Baltimore which was an unforgettable experience and one of many highlights for me here in the United States. Certainly, this thesis would have not been possible without the intellectual help and guidance throughout the year from Dr. Jin-Yeon Kim. Thank you very much for everything I learned from you during my time at Georgia Tech. Furthermore, I want to thank Dr. Rginald DesRoches for serving as a committee member.

I also want to thank Prof. Lothar Gaul and everyone at the Institut Fuer Angewandte und Experimentelle Mechanik and the office of international affairs at the University of Stuttgart for the faith in me and for giving me the opportunity to take part in this program. I also appreciate their endeavor to keep this program alive for hopefully many more years to come. I am also very thankful for the generous financial support from the DAAD.

Especially the people I met and the friends I made will make this year for ever unforgettable for me. Thanks to everyone in our lab. There was always a nice atmosphere and I had a lot of fun working with you all.

Last but not least I want to thank my family in Germany and in the United States for their support and help throughout the year. I am very happy and greatful to have such an amazing family.

TABLE OF CONTENTS

LIST OF TABLES

LIST OF FIGURES

LIST OF SYMBOLS AND ABBREVIATIONS

Symbol	Description
t_i	traction
S	surface
ρ	mass density
b_i	body force
V	volume
u_i	displacement
$\dot{u}_i$	velocity
$\ddot{u}_i$	acceleration
τ_{ij}	second order stress tensor
n_i	normal vector
ϵ_{ij}	strain tensor
C_{ijkl}	fourth order stiffness tensor
λ, μ	Lamé's parameters
E	Young's modulus
δ_{ij}	Kronecker Delta
∇	nabla operator
Φ	scalar potential
Ψ	vector potential
A, B	Amplitudes
c_L	longitudinal wave phase velocity
c_T	transversal wave phase velocity
c_R	Rayleigh wave phase velocity
$\mathbf{p}$	vector in direction of propagation
$\mathbf{d}$	vector in direction of particle motion
$\mathbf{u}$	displacement vector

Symbol	Description
t	time
k	wavenumber
Θ	Angle of incident and reflected waves
ω	angular frequency
ν	Poisson's ratio
λ	wavelength
D_L	Diffraction correction in air
D_R	Diffraction correction for Rayleigh wave and two circular transducer
J_0, J_1	Bessel functions
$H(f)$	Transfer function
S_i	signal spectrum
α	attenuation coefficient

SUMMARY

It is well known that liquid coupling agents, which are commonly used in conventional ultrasonic testing to couple an ultrasonic transducer to a solid specimen, cause a number of problems including inconsistency in results and slowness of the inspection. This is especially true when the specimen surface is rough, such as those in field concrete structures; here the solution involves time-consuming surface preparation to polish every single point of inspection, making it impractical to inspect field structures with conventional, contact methods. To address this issue, this thesis proposes a new, fully non-contact, air-coupled measurement setup in the mid to high ultrasonic frequencies (50-150 kHz). Before introducing this setup a short overview over the wave propagation theory and the attenuation of Rayleigh surface waves is given. The advanced setup and measurement technique is then presented and evaluated by calculating the signal to noise ratio for different numbers of signal averages. In addition, the effect of the lift-off distance of the transducer over the sample is also investigated. Ultrasonic waves are generated and detected in this frequency range with a sufficiently high signal to noise ratio (SNR), which enables performing a fast scan with a small number of signal averages. Using this setup, phase velocity and attenuation of Rayleigh surface waves in a concrete specimen are first measured. Then, the air coupled ultrasound technique is used to detect dicontinuities such as cracks at a concrete joint and reinforcement bars in a concrete block. Also, the capability of the proposed technique for measuring depths of surface-breaking cracks using air-coupled generated Rayleigh waves is demonstrated. Since this measurement setup directly generates Rayleigh waves, most of the disadvantages in the techniques based on the impact-echo method can be avoided and thus data processing is much simpler than that in the impact-echo based techniques. The results of the measurements show that this setup is highly promising and a big advancement towards the rapid ultrasonic nondestructive testing on large-scale field concrete structures.

CHAPTER I

INTRODUCTION

1.1 Motivation

Nondestructive testing with ultrasonic waves has great importance in the assessment of the condition of concrete structures. This method is used to detect damages or changes in the properties of the material, which might jeoperdize the durability of a structure, in an early stage. Necessary repairs can be made before the damage progresses excessive such that the repairs become very expensive. Transducers are used in the ultrasonic nondestructive testing to generate ultrasonic waves in the material. After propagating through the material this wave carries information that can be ascribed to the materials condition. Conventionally, such transducers are coupled to the specimen with a wedge in order to launch the wave in the specimen. Nondestructive evaluation techniques based on this conventional contact ultrasonic method have disadvantages due to the liquid coupling agents that are needed between the wedge and the specimen to acoustically couple the transducers to a solid specimen. The coupling is necessary in order to overcome the extremly high impedance at the air-solid interface which leads to reflection of approximatels $99,9\%$ of the ultrasonic wave. These coupling agents cause a number of problems that especially make in-service field measurement of structures impractical. Among these problems are large variabilities in results which originate from changes in the contact condition and associated amplitude variations due to the different amount of coupling agent and contact pressure between specimen and transducer. Also the slowness of inspection is a problem. The rough surface of field concrete structures requires a time consuming surface preparation, i.e., polishing every spot of inspection for repeatable measurement results. These drawbacks make the contact ultrasonic techniques inappropriate for many applications of ultrasonic testing of field concrete structures. An air-coupled generation and detection of ultrasound alleviates many of the problems caused by the liquid coupling agents. Due to their noncontact nature,

more consistent results can be obtained just by keeping the relative distances between surface and transducer constant. In addition, time consuming surface preparation is no longer necessary. This can significantly accelerate the process of field inspections and improve the measurement results. With this technique a rapid inspection of field concrete structures is now possible. The greatest problem is, however, to overcome the high impedance mismatch at the air-solid interface. Researchers have struggled in the past to generate ultrasonic waves in a concrete specimen with a fully non-contact setup with a sufficiently high signal to noise ratio. Yet, some work has already been done with non-contact ultrasonic measurements. In at al. accomplished attenuation measurements of Rayleigh wave with air coupled detection of the Rayleigh signal [6]. Stoessel was able to generate and detect ultrasound with an air-coupled setup and used this technique for applications on different materials such as wood, composite or honey comb material [23]. Kee and Zhu determined the depth of a surface breaking crack in concrete using air-coupled sensors for the signal detection [13][14]. However, the generation of the Rayleigh wave was done with a steel ball by dropping it on the surface of the specimen which in a strict sense is not a true non-contact generation. Different sizes of steel balls generated different frequencies. The non-contact detection of the wave was realized with a microphone. Castaings et al. did single sided inspection of composite materials using air-coupled ultrasound [15]. A lamb wave was used here to create a C-scan image by scanning over the surface of a plate. The week penetration of the ultrasonic wave into the material, however, has always been a problem. A sufficiently high signal to noise ratio is very important for accurat measurements. The measurement setup that is proposed in this thesis addresses this problem.

1.2 Objective

The objective is to introduce a fully air-coupled non-contact measurement setup for more consistent, more accurate, and faster measurements. Due to the impedance mismatch at the air-solid interface the intensity of the ultrasound from the generating transducer has to be strong enough such that the generated wave can be detected by a second air coupled transducer with a sufficiently high signal to noise ratio after propagating in the specimen.

This requires also a very high sensitivity for the receiving side of the setup. The higher consistency and accuracy of the measurements is achieved by the fact that the coupling agents between transducer and specimen are no longer needed. The problems due to different amounts of coupling agents and different contact pressure are eliminated. Also the surface preparation would become unnecessary and thus a time consuming step during the measurement can be saved.

1.3 Outline of this thesis

This thesis starts with an introduction to the wave propagation theory. Also the theory of the attenuation of Rayleigh waves will be discussed in detail since the measurement of the attenuation of the Rayleigh wave will be a major part of this thesis. In the following chapter the fully non-contact experimental setup to generate ultrasonic waves in concrete is presented. This setup and measurement technique is evaluated by calculating the signal to noise ratio for different numbers of signal averages. Also the effect of the lift-off distance of the transducer over the sample is investigated. Subsequently the applicability of the measurement setup for different applications is tested. Rayleigh wave attenuationa and phase velocity measurements are conductetd. Punurai et al. have shown in [27] that those parameters can be used to characterize the average size and volume fraction of entrained air voids in mortar sepcimen. This is important to determine the durability of the material. Also the issue of discontinuity detection in concrete will be addressed. Measurements to detect rebars and an artificial crack in the sample were performed and the results of these measurements will be presented. Furthermore, the procedure to characterize surface-breaking cracks in concrete with Rayleigh surface waves generated by the introduced setup will be explained. The thesis closes with possible future work and the conclusion of the work done in this thesis.

CHAPTER II

WAVE PROPAGATION THEORY

The fundamentals of wave propagataion in elastic solids will be discussed in this chapter to an extend that provides a fundamental knowledge about the concepts applied in this thesis. The equations of motions will be derived and wave phenomena based on the plane wave assumption as well as Rayleigh waves will be introduced. The theory is very well described by Achenbach in [1] and Viktorov in [25] and will be derived alongside these books.

2.1 Equations of Motion

To begin the derivation of the equations of motion we use the balance of linear momentum.

$$\int_S t_i \,\mathrm{d}S + \int_V \rho b_i \,\mathrm{d}V = \int_V \rho \ddot{u}_i \,\mathrm{d}V, \tag{1}$$

where t_i is the traction on the surface S, ρ the mass density, b_i a body force on the volume V and $\ddot{u}_i$ an acceleration. After using the Cauchy formula

$$t_i = \tau_{ji} n_i, \tag{2}$$

where τ_{ji} is the second order stress tensor and n_i is the normal vector, to replace the traction vector we can apply the divergence theorem and the balance of linear momentum can be written as one volume integral

$$\int_V \tau_{ji,i} + \rho b_i - \rho \ddot{u}_j \mathrm{d}V = 0. \tag{3}$$

This expression has to hold true for any arbitrary volume V, therefore, the equation of motion is

$$\tau_{ji,i} + \rho b_i - \rho \ddot{u}_j = 0. \tag{4}$$

For some cases it is more convinient to write the equation of motion only in dependence of the displacement u_i. Following are the necessary steps to obtain the equation of motion

in dependence of the displacement. The fourth order tensor C describes the relationship between the stress and the strain:

$$\tau_{ij} = C_{ijkl}\epsilon_{kl}. \tag{5}$$

For a homogenous, isotropic, elastic medium the tensor C can be expressed as

$$C_{ijkl} = \lambda\delta_{ij}\delta_{kl} + \mu(\delta_{ik}\delta_{jl} + \delta_{il}\delta_{jk}) \tag{6}$$

where

$$\lambda = \frac{E\nu}{(1+\nu)(1-2\nu)} \tag{7}$$

and

$$\mu = \frac{E}{2(1-\nu)} \tag{8}$$

are the Lamé's parameters and δ is the Kronecker Delta. Combining Eq. (6) and Eq. (5) gives us Hooke's law

$$\tau_{ij} = \lambda\epsilon_{kk}\delta_{ij} + 2\mu\epsilon_{ij}. \tag{9}$$

The strain is defined by

$$\epsilon_{ij} = \frac{1}{2}(u_{ji} + u_{ij}). \tag{10}$$

With Eq. (10), Hooke's law and by neglecting the body forces in Eq. 4, we obtain Navier's equation of motion independent of the stress tensor with

$$\rho\ddot{u}_i = (\lambda+\mu)u_{j,ji} + \mu u_{i,jj}. \tag{11}$$

Using vector notation instead of the Einstein summation notation, Eq. (11) can be written as

$$\rho\ddot{u} = (\lambda+\mu)\nabla\nabla\cdot u + \mu\nabla^2 u, \tag{12}$$

with ∇ as the nabla operator. This wave equation describes the motion of both the longitudinal and transversal wave. Since both waves propagate independently it is desirable to

seperate the wave equation using potential functions. This is possible with the Helmholtz decomposition:

$$\vec{u} = \vec{\nabla}\Phi + \vec{\nabla} \times \vec{\Psi}. \tag{13}$$

Φ is the scalar potential and Ψ is the vector potential in this expression. Substituting Eq. (13) into Eq. (12) and using the identities that

$$\nabla \cdot \nabla\Phi = \nabla^2\Phi \tag{14}$$

and

$$\nabla \cdot \nabla \times \Psi = 0 \tag{15}$$

yields to

$$\nabla[(\lambda + 2\mu)\nabla^2\Phi - \rho\ddot{\Psi}] + \nabla \times [\mu\nabla^2\Psi - \rho\ddot{\Psi}] = 0. \tag{16}$$

This equation is satisfied if

$$\nabla^2\Phi = \frac{1}{c_L^2}\ddot{\Phi} \tag{17}$$

and

$$\nabla^2\Psi = \frac{1}{c_T^2}\ddot{\Psi} \tag{18}$$

where $c_L = \sqrt{\frac{\lambda+2\mu}{\rho}}$ and $c_T = \sqrt{\frac{\mu}{\rho}}$ are the velocity of the longitudinal and transvere waves, respectively.

2.2 Wave Phenomena

To describe plane waves the assumptions are made that strain ϵ, stress τ and displacement $\mathbf{u}$ are constant on a plane perpendicular to it's direction of propagation $\mathbf{p}$. $\mathbf{d}$ is the vector in direction of the particle motion. $\mathbf{p}$ and $\mathbf{d}$ are unit vectors. The displacement of such a wave can be described with

$$\mathbf{u} = f(x \cdot \mathbf{p} - ct)\mathbf{d}, \tag{19}$$

where c denotes the velocity and can either be from the longitudinal (c_L) or transveres (c_T) wave. By substituting Eq. (19) into Eq. (12) we obtain

$$(\mu - \rho c^2)\mathbf{d} + (\lambda + \mu)(\mathbf{p} \cdot \mathbf{d})\mathbf{p} = 0. \tag{20}$$

With $\mathbf{d}$ and $\mathbf{p}$ being two different vectors, Eq. (20) is satisfied by either $\mathbf{d} = \pm\mathbf{p}$ or $\mathbf{d} \cdot \mathbf{p} = 0$. The solution $\mathbf{d} = \pm\mathbf{p}$ implies that the particle motion is parallel to the propagation direction. This is the characteristic of the longitudinal wave and equation Eq. (20) becomes the speed of the latter mentioned wave with

$$c_L = \sqrt{\frac{\lambda + 2\mu}{\rho}} \tag{21}$$

For $\mathbf{d} \cdot \mathbf{p} = 0$ the particle movement is orthogonal to the direction of propagation. Eq. (20) becomes in this case

$$c_T = \sqrt{\frac{\mu}{\rho}}, \tag{22}$$

which is the speed of the transverse wave.

2.2.1 Reflection of plane waves

The wave phenomena described above propagate independently in infinite media. However, if the media is finite and boundaries exist, reflection and transmission of the propagating wave will occur. Considering a stress free boundary, only reflections and no transmission occurs. A stress free boundary exist between a solid medium and vacuum. Considering a wave propagating in the x_1x_2-plane and a boundary along the x_1-axis, the boundary conditions are $\sigma_{22} = 0$ and $\sigma_{12} = 0$. For P-wave and SV-waves a mode conversion occurs at the boundary which leads to both a reflected P-wave and SV-wave as shown in Figure 2.1. For a SH-wave no mode conversion occurs and only a SH-wave will be reflected.

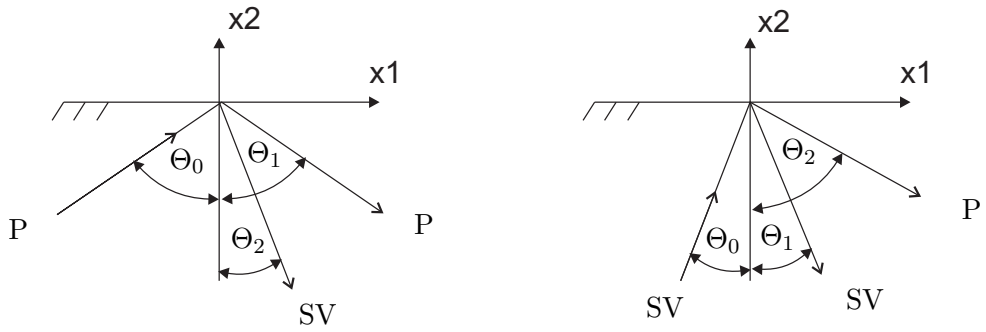

Figure 2.1: Reflection p and sv wave.

A relationship can be established between the incident angle Θ_0 and the reflected angles Θ_1 and Θ_2 if the freqeuncy of the incident wave and the reflected waves is linear and constant.

Table 2.1: Relationship between incident and reflected angle.

Incident Θ_0	Reflected P Θ_1	Reflected SV Θ_2
P	$\Theta_1 = \Theta_0$	$sin\Theta_2 = \frac{c_T}{c_L} sin\Theta_0$
SV	$sin\Theta_1 = \frac{c_T}{c_L} sin\Theta_0$	$\Theta_2 = \Theta_0$

These angles also satisfy Snell's law. Therefore, it can be written,

$$k_0 sin\Theta_0 = k_1 sin\Theta_1 = k_2 sin\Theta_2. \tag{23}$$

Two cases exist for which no mode conversion occurs altough a P-wave or SV-wave reach a boundary in a finite medium with stress free boundary conditons.

- The incident wave is orthogonal to the boundary ($\Theta_0 = 0$). The wave will be reflected in the same angle and no mode conversion will occur.
- For incident angles of the P-wave greater the the critical angle. This critical angle is calculated with $\Theta_{critical} = sin^{-1}\left(\frac{c_T}{c_L}\right)$. In theses cases, only a SV-wave is reflected and the P-wave generates a Rayleigh wave that propagates on the surface of the medium.

2.3 Rayleigh Surface Wave

The theory of Rayleigh surface waves is very well described in [25] and [20]. Alongside these publications the follwing summary of the most important equations describing the Rayleigh wave is carried together.

Rayleigh surface waves propagate on the surface of elastic half spaces and decay with distance from this surface with depth. To start the derivation of the equations that describe the charcteristics of this wave we consider the two-dimensional case of plane waves in a homogeneous, isotropic solid, where the displacment vector can be written with the Helmholtz decomposition through potentials as

$$\vec{u} = \vec{\nabla}\Phi + \vec{\nabla} \times \vec{\Psi}. \tag{24}$$

These two potentials enable us to seperate Navier's governing wave equation into two wave equations as already mentioned earlier. For the longitudinal wave with

$$\nabla^2\Phi - \frac{1}{c_L^2}\frac{\partial^2\Phi}{\partial t^2} = 0 \tag{25}$$

and for the shear wave the equation can be written as

$$\nabla^2\vec{\Psi} - \frac{1}{c_T^2}\frac{\partial^2\vec{\Psi}}{\partial t^2} = 0. \tag{26}$$

c_L and c_T are the longitudinal and shear wave velocities, respectively.

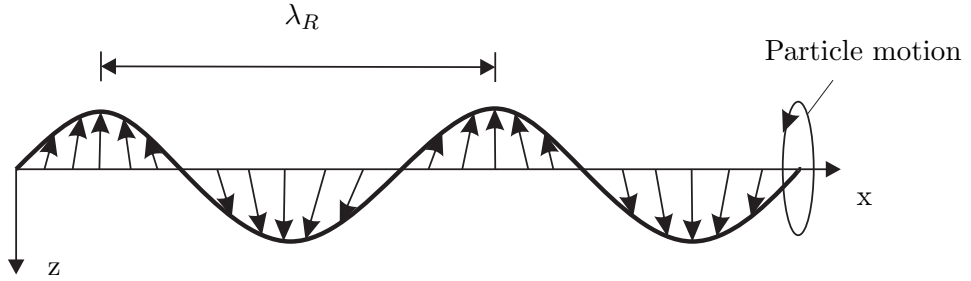

Figure 2.2: Coordinate system as used in the derivations of the equations describing Rayleigh wave.

Assuming that the Rayleigh wave propagates according to the coordinate system in Figure 2.2 along the surface in x-direction, decaying with depth in z-direction and having

no dependence in the y-direction, the displacement vector is

$$\vec{u} = \begin{pmatrix} u \\ 0 \\ w \end{pmatrix} \tag{27}$$

and all derivatives with respect to y are zero. Therefore we get only one nonzero component for the vector potential

$$\vec{\Psi} = \begin{pmatrix} 0 \\ \Psi \\ 0 \end{pmatrix}. \tag{28}$$

Eq. (25) and Eq. (26) can therefore now be written as

$$\frac{\partial^2 \Phi}{\partial x^2} + \frac{\partial^2 \Phi}{\partial z^2} - \frac{1}{c_L^2}\frac{\partial^2 \Phi}{\partial t^2} = 0 \tag{29}$$

$$\frac{\partial^2 \Psi}{\partial x^2} + \frac{\partial^2 \Psi}{\partial z^2} - \frac{1}{c_T^2}\frac{\partial^2 \Psi}{\partial t^2} = 0. \tag{30}$$

To solve these equations we seek a solution of the form

$$\Phi = F(z)e^{i(k_R x - \omega t)} \tag{31}$$

and

$$\Psi = G(z)e^{i(k_R x - \omega t)}. \tag{32}$$

where $k_R = \frac{\omega}{c_R}$ is the wavenumber of the Rayleigh wave which is propagating in x direction and the amplitude is only a function of z. Choosing this solution we set the longitudinal and transversal wave to propagate at the same velocity, the velocity of the Rayleigh wave c_R. This is a requirement for the Rayleigh wave to exist. Pluggig Eq. (31) in Eq. (29) and Eq. (32) in Eq. (30) yields to

$$\frac{\partial^2 F(z)}{\partial z^2} - (k_R^2 - k_L^2)F(z) = 0 \tag{33}$$

and

$$\frac{\partial^2 G(z)}{\partial z^2} - (k_R^2 - k_T^2)G(z) = 0, \tag{34}$$

with $k_T = \frac{\omega}{c_T}$ and $k_L = \frac{\omega}{c_L}$. In order of those equations to be satisfied $F(z)$ has to be $A \cdot e^{\pm\sqrt{k_R^2 - k_L^2}z}$ and $G(z)$ has to be $B \cdot e^{\pm\sqrt{k_R^2 - k_T^2}z}$ with A and B being arbitrary constants. It can be shown that $k_R > k_T > k_L$. This means for a positive root in the exponent the motion would increase with depth. However, the characteristicum of a Rayleigh surface waves is the decay of motion with depth. Therefore, Φ and Ψ are

$$\Phi = Ae^{-qz}e^{i(k_R x - \omega t)} \tag{35}$$

$$\Psi = Be^{-sz}e^{i(k_R x - \omega t)} \tag{36}$$

with $q = \sqrt{k_R^2 - k_L^2}$ and $s = \sqrt{k_R^2 - k_T^2}$. To get a relation between the constants A and B and the wavenumber k_R we impose the boundary conditions that the stresses σ_{zz} and σ_{xz} must be zero at $z = 0$, the surface of the half space in which the Rayleigh wave propagates. The stress components are

$$\sigma_{xx} = \lambda\left(\frac{\partial^2\Phi}{\partial x^2} + \frac{\partial^2\Phi}{\partial z^2}\right) + 2\mu\left(\frac{\partial^2\Phi}{\partial z^2} + \frac{\partial^2\Psi}{\partial x \partial z}\right) \tag{37}$$

and

$$\sigma_{xz} = \mu\left(2\frac{\partial^2\Phi}{\partial x \partial z} + \frac{\partial^2\Psi}{\partial x^2} - \frac{\partial^2\Psi}{\partial z^2}\right) \tag{38}$$

with λ and μ being the Lamè constants. This will lead us eventually after some calculations and transformations to the potentials

$$\Phi = -Ae^{-qz}e^{i(k_R x - \omega t)} \tag{39}$$

$$\Psi = iA\frac{2k_R q}{k_R^2 + s^2}e^{-sz}e^{i(k_R x - \omega t)} \tag{40}$$

We can now also get the characteristic equation that determines k_R:

$$4k_R^2 qs - (k_R^2 + s^2)^2 = 0. \tag{41}$$

After a transformation Eq. (41) reduces to

$$\eta^6 - 8\eta^4 + 8(3 - 2\xi^2)\eta^2 - 16(1 - \xi^2) = 0 \tag{42}$$

with $\eta = \frac{k_T}{k_R}$ and $\xi = \frac{k_L}{k_T}$. This equation is called *the Rayleigh wave equation.* Six solutions exist for this equation. However, only the solutions lying between 0 and 1 correspond to the Rayleigh surface save and for a Poission ratio ν between 0 and 0.5 only one such solution exists. An approximation of this solution is proposed by Viktorov in [25] with

$$\eta_R = \frac{0.87 + 1.12\nu}{1 + \nu} \tag{43}$$

or

$$c_R = \frac{0.87 + 1.12\nu}{1 + \nu} c_L. \tag{44}$$

This equation gives the value of the Rayleigh wave velocity for different Poisson ratios ν. For ν between 0 and 0.5 the phase velocity c_R varies between $0.87c_L$ and $0.96c_L$. The expression for the velocity of the Rayleigh wave does not depend on the frequency. The Rayleigh wave is thus nondispersive. To get the displacement in u and w direction we write Eq. (24) as

$$u = \frac{\partial \Phi}{\partial x} - \frac{\partial \Psi}{\partial z} \tag{45}$$

$$w = \frac{\partial \Phi}{\partial z} + \frac{\partial \Psi}{\partial x} \tag{46}$$

and plug in the potentials Φ and Ψ that we just obtained.

$$u = Ak_R(e^{-qz} - \frac{2qs}{k_R^2 + s^2} e^{-sz}) e^{k_R x - \omega t} \tag{47}$$

$$w = Aq(e^{-qz} - \frac{2k_R^2}{k_R^2 + s^2} e^{-sz}) e^{k_R x - \omega t}. \tag{48}$$

From this equations it can also be shown that the Rayleigh wave propagates on the surface in an elliptical form. Normalizing the displacements with respect to the constant A we obtain

$$\bar{u} = \frac{u}{A} = k_R(e^{-qz} - \frac{2qs}{k_R^2 + s^2} e^{-sz}) e^{k_R x - \omega t} \tag{49}$$

$$\bar{w} = \frac{w}{A} = q(e^{-qz} - \frac{2k_R^2}{k_R^2 + s^2} e^{-sz}) e^{k_R x - \omega t}. \tag{50}$$

The vector sum of u and v leads now to the equation of the ellipse that decribes the pattern of the propagation of the wave:

$$\frac{\bar{u}^2}{k_R^2(e^{-qz} - \frac{2qs}{k_R^2+s^2}e^{-sz})^2} + \frac{\bar{w}^2}{q^2(e^{-qz} - \frac{2k_R^2}{k_R^2+s^2}e^{-sz})^2} = 1. \tag{51}$$

CHAPTER III

ATTENUATION

One part of this thesis is the attenuation and phase velocity measurement of a Rayleigh wave on a concrete specimen with the non contact air-coupled setup that will be introduced in the next chapter. Therefore, an overview of the theoretical and experimental background of the attenuation of Rayleigh waves will be given in this chapter.

3.1 Attenuation coefficient of Rayleigh surface waves

The results we obtained in the latter section do not consider the attenuation of the Rayleigh wave. By using the *correspondance principle* [25] we can account for attenuation in viscoelastic materials. The *correspondance principle* can be applied by adding an imaginary part to the wavenumber and thus making it a complex quantity. This imaginary part is called the attenuation coefficient. The attenuation coefficient decribes the amplitude reduction o waves during propagtaion and is frequency dependent. It is either given in nepers $[Np]$ per unit lenght or decibles $[dB]$ per unit length. In the expression for the Rayleigh surface wave we have a Rayleigh wavenumber as well as longitudinal and shear wavenumbers. We write these in a complex form and obtain

$$\begin{aligned} \bar{k}_L &= k'_L + ik''_L, \\ \bar{k}_T &= k'_T + ik''_T, \\ \bar{k}_R &= k'_R + ik''_R. \end{aligned} \tag{52}$$

The imaginary part of the wavenumber is assumed to be much smaller than the real part. This means the attenuation is relatively small so that the wave can propagate at least as much as a few wavelength. Let us write the wavenumbers as follows

$$\begin{aligned} \bar{k}_L &= k'_L(1 + i\delta), \\ \bar{k}_T &= k'_T(1 + i\beta), \\ \bar{k}_R &= k'_R(1 + i\gamma) \end{aligned} \tag{53}$$

where $\delta = \frac{k_L''}{k_L'}$, $\beta = \frac{k_T''}{k_T'}$ and $\gamma = \frac{k_R''}{k_R'}$. δ, β and γ are factors on the imaginary part of the wavenumbers to express the attenuation coefficients k_L'', k_T'' and k_R''. With the charcteristic equation Eq. (42) which we obtained earlier, we can now find an expression for γ to be able to get the attenuation coefficient of the Rayleigh wave. With $\bar{\eta}^2 = \frac{\bar{k}_s^2}{\bar{k}_R^2}$ and $\bar{\xi}^2 = \frac{\bar{k}_p^2}{\bar{k}_s^2}$ the characteristic eqution can be written as

$$\bar{\eta}^6 - 8\bar{\eta}^4 + 8(3 - 2\bar{\xi}^2)\bar{\eta}^2 - 16(1 - \bar{\xi}^2) = 0. \tag{54}$$

Plugging the wavenumbers from Eq. (53) in the expressions for $\bar{\eta}^2$ and $\bar{\xi}^2$ and substituting those into the characteristic equation Eq. (54) gives us

$$\begin{aligned}\left(\frac{k_T'(1+i\beta)}{k_R'(1+i\gamma)}\right)^6 - 8\left(\frac{k_T'(1+i\beta)}{k_R'(1+i\gamma)}\right)^4 + 8\left(3 - 2\left(\frac{k_L'(1+i\delta)}{k_T'(1+i\beta)}\right)^2\right) \times \\ \left(\frac{k_T'(1+i\beta)}{k_R'(1+i\gamma)}\right)^2 - 16\left(1 - \left(\frac{k_L'(1+i\delta)}{k_T'(1+i\beta)}\right)^2\right) = 0.\end{aligned} \tag{55}$$

Finally, after doing some algebraic manipulations we get an expression for γ with

$$\gamma = A\delta + (1 - A)\beta \tag{56}$$

where

$$A = \frac{16\xi'^2(1 - \eta'^2)}{\eta'^2(3\eta'^4 - 16\eta'^2 - 16\xi'^2 + 24)} \tag{57}$$

and

$$\begin{aligned}\xi' &= \frac{k_L'}{k_T'} \\ \eta' &= \frac{k_L'}{k_R'}.\end{aligned} \tag{58}$$

The full expression for the imaginary part of the Rayleigh wavenumber and therefore the Rayleigh surface wave attenuation coefficient is

$$k_R'' = \gamma k_R' = (A\delta + (1 - A)\beta)\, k_R'. \tag{59}$$

This equations shows that the Rayleigh wave attenuation coefficient depends on both the attenuation coefficient of the longitudinal wave (δ) and shear wave (β).

A only depends on the Poisson's ratio ν. Fig. 3.1 shows both A and $1 - A$ over the Poisson's ratio.

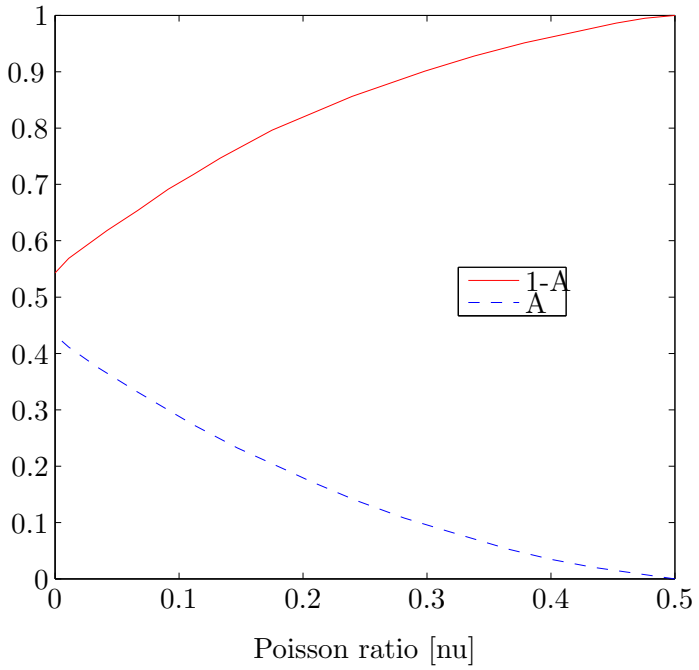

Figure 3.1: A and $1 - A$ over the Poisson ratio ν [25]

It can be seen that A is a small quantity and, therefore the contribution to the attenuation coefficient from the shear wave with β is bigger than the one from the longitudinal wave with δ. In Table 3.1 A is given for different materials

Table 3.1: A for different materials.

Material	Poisson's ratio	A
Concrete	0.2	0.19
Steel	0.27	0.11
Aluminum	0.33	0.07
Rubber	0.5	0

The longitudinal attenuation factor has in concrete, the material of the specimens in this thesis, the greatest contribution towards the total attenuation factor.

3.2 Experimental determination of the attenuation coefficient in concrete specimen

Attenuation is the decay of the amplitude of a propagating wave. The measured attenuation in experiments consists not only of the physical meaningful intrinsic attenuation but also of the extrinsic attenuation which is due to the applied measurement method and has nothing to do with the physical properties of the material. Both the extrinsic and intrinsic attenuation will now be described in more detail before the experimental procedure of obtaining the attenuation and phase velocity will be discussed.

Extrinsic attenuation The transmitted wave gets first attenuated when leaving the transducer. The wave beam starts to spread while propagating in the specimen which causes the pressure of the wave to drop [17]. Punurai [18] has shown that this effect can be decreased by increasing the ratio of the diameter of the transducer to the wavelength which results in a less divergent wave field and thus less attenuation. This spreading of the wave is called diffraction and needs to be taken into account in the attenuation measurement of the specimen. A correction of this effect in longitudinal waves is proposed by Rogers and van Buren in [19] with

$$D_L = 1 - e^{\frac{-2\pi}{s}i}\left[J_0\left(\frac{2\pi}{s}\right) + iJ_1\left(\frac{2\pi}{s}\right)\right] \tag{60}$$

if the transducers are circular as it is the case in our experimental setup. Here s is the normalized distance that is defined as $l/\frac{a^2}{\lambda}$ where l is the distance from the transducer, a the radius of the transducer, and λ the wavelength of the propagating wave. J_0 and J_1 are the zeroth and first order Bessel functions of the first kind. However, due to the way we will carry out the measurements we can neglect this effect. The wave propagates only a very small distance in the air before reaching the specimen. Also, we measure the attenuation, as will be seen later, by using the decay of the amplitude of the Rayleigh wave after propagating over different distances in the concrete. The contribution due to the diffraction in the air will be the same, however, the diffraction occuring on the surface on which the Rayleigh wave is propagating has to be corrected. This is done by a diffraction correction that is proposed by Ruiz and Nagy in [21] and modified by In et al. in [6] for

two circular transducer. The equation is

$$D_R(\zeta) = \sqrt{\frac{s}{2\pi i}}\frac{1}{2}\int_{-1}^{1} cos(\xi\frac{\pi}{2})\,\mathrm{d}\xi \int_{-1}^{1} cos(\xi'\frac{\pi}{2}) \times \frac{e^{is(\sqrt{(\xi-\xi')^2+\zeta^2}-\zeta)}}{\sqrt[4]{(\xi-\xi')^2+\zeta^2}}\mathrm{d}\xi'. \tag{61}$$

$\zeta = \frac{z}{a}$, $\xi = \frac{x}{a}$, $\xi' = \frac{x'}{a}$ and $s = ak = \frac{2\pi a}{\lambda}$ is the normalized frequency or the normalized source size by wavelength. z is the direction of the propagation of the Rayleigh wave on the surface and x is perpendicular to the z direction in the same plane as the surface of the specimen. Figure 3.2 taken from [21] shows the used coordinate system.

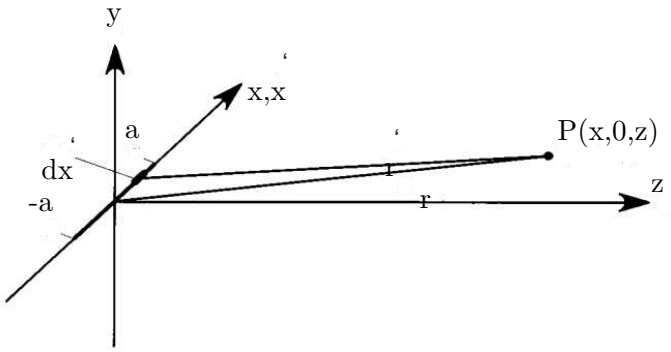

Figure 3.2: Coordinate system used by Ruiz and Nagy in [21] for the diffraction correction.

This diffraction correction will account for the diffraction loss that occurs while the Rayleigh wave propagates in the specimen.

Intrinsic attenuation Intrinsic attenuation is the attenuation within the specimen as the name already reveals. The intrinsic attenuation contains the important physical information that are used to characterize the material. In general it can be divided into two causes. One of those is the internal absorption by the material. Internal absorption occurs when a part of the energy of the wave is absorbed by the material and transferred into heat. Thus, the energy of the wave is transformed into another form of energy and the wave gets attenuated. Scattering is the part of intrinsic attenuation that is caused by inhomogeneity in the specimen. Aggregates, grains, and inclusions have elastic properties different from those of the cement matrix, which leads to scattering of the waves that are propagating through the specimen. Due to scattering, wave energy propagates in directions different

from the original direction of incidence. This makes it look like the wave is attenuated and its amplitude is reduced even when there is no change in the total energy. This attenuation caused by scattering is frequency-dependent. Depending on the frequency region, the attenuation has a different dependency on the frequency. These regions are characterized by the properties of the material and especially by the representative dimesnion (e.g. radius) d of the aggregate/scatterers in the specimen. Three different regimes are distinguished as shown in Table 3.2 [26, 27].

Table 3.2: Scatter regimes

Regime	Frequency dependency	Range
Rayleigh Regime	$\alpha(f) \propto f^4 \cdot d^3$	$2\pi d/\lambda \ll 1$
Stochastic Regime	$\alpha(f) \propto f^2 \cdot d^1$	$2\pi d/\lambda \approx 1$
Geometric Regime	$\alpha(f) \propto d^{-1}$	$2\pi d/\lambda > 1$

3.2.1 Attenuation coefficient and phase velocity

For two circular transducers, we can write the amplitude spectra of the measured signal as

$$S_i(f) = S_0(f)H(f) \tag{62}$$

where $H(f)$ is a transfer function, $S_0(f)$ is the spectrum of the input signal. The full expression for the transfer function for a wave propagating in z direction is

$$H(f) = D_R(z)e^{-\alpha(f)z}e^{i(\omega t - k(f)z + \Phi_0)}, \tag{63}$$

wkere $D_R(z)$ is the diffraction correction, $\alpha(f)$ the attenuation coefficient, $k(f) = \frac{\omega}{c_R(f)}$ the real part of the wavenumber, and Φ_0 is the phase angle of the source signal. Relating this form to the notation we used for the derivation of the analytical solution for the attenuation coefficient in of the Rayleigh surface wave in chapter 1, we get

$$\begin{aligned} \alpha(f) &= Im(\bar{k}_R) = \gamma k'_R \\ k(f) &= Re(\bar{k}_R) = k'_R \end{aligned} \tag{64}$$

and we can write the whole expression for the amplitude spectra in the frequency domain as

$$S_i(f) = S_0(f) D_R(z) e^{-(\gamma k'_R(f))z} e^{i(\omega t - k'_R(f) z + \Phi_0)}. \tag{65}$$

If we take the ratio of the amplitude spectra of two signals measured at two distances z_1 and z_2 we get

$$\frac{S_1}{S_2} = \frac{D_1}{D_2} e^{-\gamma k'_R(z_2 - z_1)} e^{-ik'_R(z_2 - z_1)}. \tag{66}$$

Taking the magnitude of Eq. (66) leads to

$$\left|\frac{S_1}{S_2}\right| = \left|\frac{D_1}{D_2}\right| e^{-\gamma k'_R(z_2 - z_1)}. \tag{67}$$

Subsequently we take the logartithm of Eq. (67) and we obtain

$$ln\left|\frac{S_1}{S_2}\right| = ln\left|\frac{D_1}{D_2}\right| - \gamma k'_R(z_2 - z_1). \tag{68}$$

After solving for $\gamma k'_R$ we get the expression for the attenuation coefficient with

$$\gamma k'_R(f) = \alpha(f) = \frac{ln\left(\frac{D_R(z_1)}{D_R(z_2)}\right) - ln\left(\frac{S_1(f)}{S_2(f)}\right)}{z_2 - z_1}. \tag{69}$$

The expression for the phase velocity of the Rayleigh wave can be obtained by taking the argument of Eq. (66)

$$Arg\left[\frac{S_1}{S_2}\right] = Arg\left[\frac{D_1}{D_2}\right] - \frac{\omega}{c_R}(z_2 - z_1). \tag{70}$$

Solving for c_R finally leads to

$$c_R(f) = \frac{2\pi f(z_2 - z_1)}{Arg\left[\frac{D_1}{D_2}\right] - Arg\left[\frac{S_1}{S_2}\right]}. \tag{71}$$

[22]

CHAPTER IV

EXPERIMENTAL SETUP

4.1 Benefits of a fully noncontact measurement setup

In experimental examination of concrete with ultrasound usually coupling agents are used to couple the transducers to a solid specimen. These coupling agents that on one hand help overcome the high impedance between the air and the specimen are causing problems on the other hand that influence the quality of the measurements in terms of consistency and lead to more time consuming procedures to collect the data.

A non contact measurement setup in which the transducers are coupled to the specimen only through the air would alleviate the issues caused by the liquid coupling agents. The non contact setup is easy to install for in field measurements and measurements can be taken over a large area in a fraction of the time that would be necessary with the convetional contact method. Due to the high impedance mismatch between air and the concrete specimen a special experimental setup is necessary. An ultrasonic signal that is strong enough to generate a wave in the concrete specimen, despite more than 99.9 % of the incident signal gets reflected at the surface, has to be transmitted from the transducer and the detection has to be sensitive enough to detect the signal after it propagated through the specimen.

4.2 Development of the setup

Crucial for the success of the setup is a suffcient amplification of signals. High amplification of the signal strength leads usually also to an amplification of the noise. Therefore, simple amplification of the signal in one step will not have the desired effect. For a good signal to noise ratio the signal has to be in a stronger amplified than the noise. Realising this amplification in two steps with two amplififer that are connected in series leads to the the higher signal to noise ratio that is needed for the applicability of this setup for ultrasonic measurements.

4.3 The setup for fully noncontact measurements

The setup is for all experiments identical on the receiving side, however, changes are made on the transmitting side of the setup for the surface-breaking crack experiment. The schematic of the setup is shown in Figure 4.1.

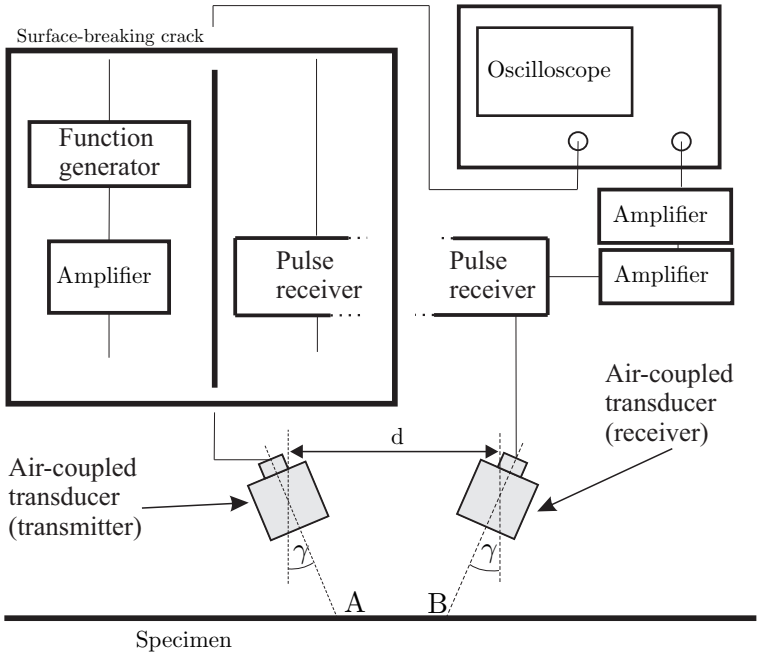

Figure 4.1: Schematic of the experimental setup.

For all experiments, besides the surface-breaking crack characterization, the transmitter is connected to a pulse receiver. The signal is amplified by a total of 81 dB to be able to detect the ultrasonic signals with a sufficient signal-to-noise ratio (SNR). The first amplifcation is done by the pulse receiver with $30dB$. On this amplification of the transmitted signal follows the amplification on the receiving side. The signal is amplified in two steps with two amplifiers that are connected in series. The signal is amplified in a first step with $31dB$ before another amplification with $20dB$ follows. For the surface-breaking crack experiment the connection of the transmitter is changed as shown in Figure 4.1. The pulse receiver is replaced by a function generator and an extra amplifier to amplify the transmitted signal. This is done to be able to generate signals with different frequencies. The signal is amplified with $50dB$ before it is transmitted which makes a total amplification of $101dB$ in this case.

4.4 Transducers

The transducers used for this setup are NCG50 non-contact transducer from the Ultran Group. The same kind of $100kHz$ transducers are used for all experiments. The transducers always operate in a pitch catch mode, where the transmitter sends out a short signal that generates a wave in the specimen which is then received by the second transducer. It is important to shield the receiving transducer from the air-borne acoustic signal that is emitted from the transmitter and propagates through the air. An acoustic barrier has to be placed between the transducers to minimize the reception of this acoustic signal by the receiver. In the measurements described in this thesis, a thick plastic sheet is used in between the transducers and the small gaps between the sheet and the rough concrete surface are closed with a tape.

4.4.1 Mounting

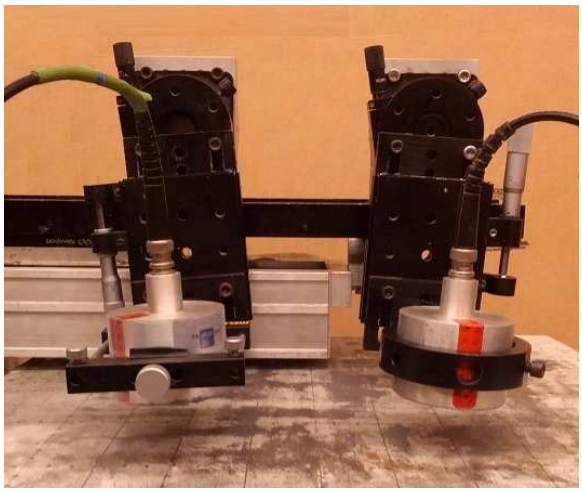

Figure 4.2: Transmitter and receiver.

The mounting of the transducers shown in Figure 4.2 is important since the orientation of the transducers in respect to surface of the specimen is a crucial part for the success of the measurements. The transducers are fixed in mountings that are rotatable to adjust the angles for the measurements and also adjustable in height. For the the scanning of the surface to image the discontinuites the setup of the mounting is designed to move the

transducer in a two dimensional plane over the surface of the specimen.

4.4.2 Signal to Noise Ratio (100kHz transducer)

Figure 4.3 shows the signal-to-noise ratio and the time duration in seconds to obtain the averaged waveform. It can be seen that for the number of averages that is higher than 256, the signal-to-noise ratio does not increase significantly anymore while the time to obtain the signal increases drastically (SNR=31.52dB for 256 averages). Therefore, 256 signals are averaged to obtain the waveforms. The signal to noise ratio

$$SNR_{dB} = 20 \log_{10} \left(\frac{A_{signal}}{A_{noise}} \right) \tag{72}$$

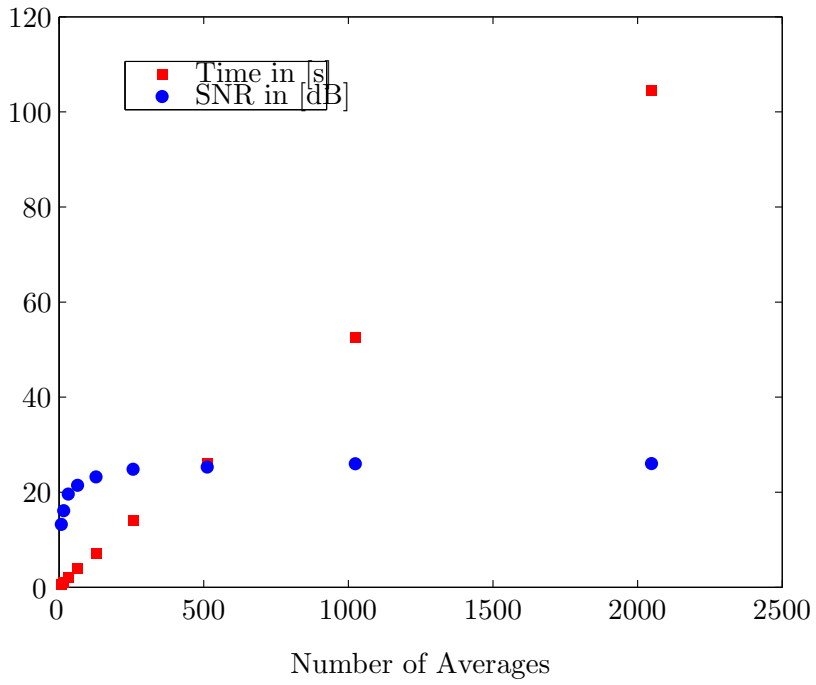

Figure 4.3: Signal to noise ration n [dB] and time to obtain a signal in [s] over number of averages.

4.4.3 Lift-off Distance (100kHz transducer)

The process of installing the measurement setup led to question of whether or not there is an ideal lift-off distance for the transducers with which the measured signal becomes stronger. To determine the effect of the lift-off distance Rayleigh surface wave measurements are

performed with different distances between the transducers and the surface of the sample. Fig. 4.4 shows the measured Rayleigh wave signals for lift-off distances between $1cm$ and $3.5cm$.

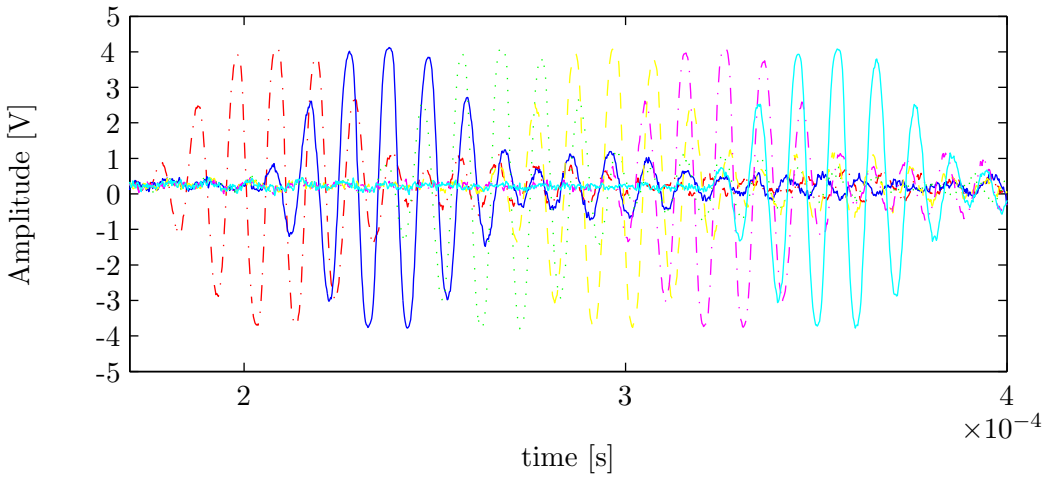

Figure 4.4: Time signal of a Rayleigh wave for different lift-off distances ($1cm$, $1.5cm$, $2cm$, $2.5cm$, $3cm$ and $3.5cm$ from left to right).

The effect of the lift-off distance is reflected in the different arrival times of the signals, however, no changes in the height of the amplitudes are recognizable. It can be seen that the effect of different lift-off distances on the strength of the detected signal can be neglected, if it at all exists. Table. 4.1, which lists the values of the maximal amplitude of the signals, confirms this observation.

Table 4.1: Maximal amplitude of the Rayleigh waves for different lift-off distances.

Lift-off distance [cm]	Amplitude [V]
1	4.11
1.5	4.13
2	4.12
2.5	4.11
3	4.22
3.5	4.10

The lift-off distance is therefore insignificant in the frequency range of the transducers that are used for the experiments. It is therefore not necessary to keep the transducers at a specific distance to the sample. This is very important since in many practical situations, it is difficult to keep the transducer-to-specimen distance constant for many reasons.

CHAPTER V

SPECIMENS

Two different specimens are used for the experiments in this thesis. The attenuation and phase velocity measurements are carried out on the same specimen as the dicontinuity detection. For the surface-crack characterization a different concrete sample is used.

5.1 Specimen 1

Fig. 5.1 shows the concrete specimen that is used for the discontinuity detection as well as for the attenuation and phase velocity measurements of the Rayleigh wave. It is made out of type I-II cement with a water-to-cement ratio of 0.53. Coarse #57 stone aggregate is used as well as fine aggregate which is a mixture out of natural and manufactured sand. The specimen and form is covered with a plastic sheet in order to maintain the moisture for the first 24h of the curing process. After 24 hours, the plastic sheet and the forms were removed, and the specimen was moved into the fog room for 40 days. The fog room is maintained at a temperature of 70 4 deg F and 100% humidity. The specimen contains four steel reinforcement bars as well as an artificial crack that goes halfway through the width of the specimen as shown in Fig. 5.2. The crack was created by leaving a plastic sheet in the wet concrete. The plastic sheet was besmeared with grease to easily remove it after the concrete has cured.

Figure 5.1: Concrete specimen with reinforcement bars and artificial crack.

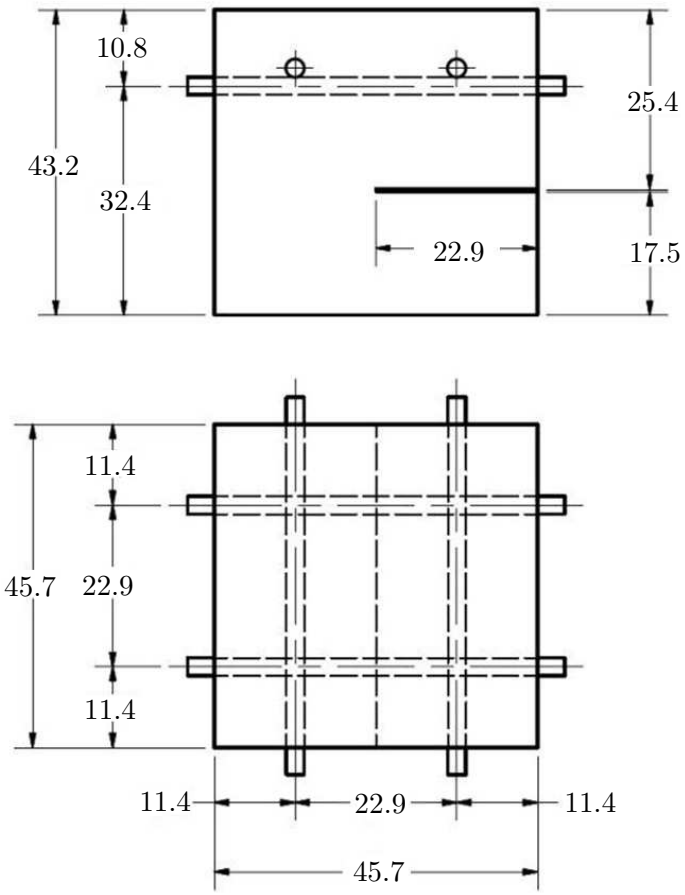

Figure 5.2: Dimensions of the concrete sample in [cm].

In order to interprete the attenuation measurement results with the different scattering

regimes introduced in 3.2, it is important to know the size of the aggregates used in this concrete sample. Table 5.1 shows the sieve analysis of #57 aggregate, where the distribution of the different sizes of the aggregates in the sample are listed.

Table 5.1: Sieve analysis aggregate #57 [2].

Sieve size [cm]	Percent Passing [%]
$2''$	100
$1\ 1/2''$	100
$1''$	98
$3/4''$	89
$1/2''$	39
$3/8''$	19
#4	3
#8	1.5

The actual average size of the aggregates near the surface of the concrete specimen where the Rayleigh wave propagates cannot be exactly determined. However, we know that during the curing process especially big stones and in general stones of the #57 aggregate, which is embedded in the cement matrix, sink down and the aggregate density decays therefore towards the surface. Also the relatively high mass fraction of the fine aggregate lowers the average size of the stones. An average stone size between 0.5 cm and 0.8 cm seems therefore to be realistic. The wavelengths in the considered frequency range from $50kHz$ to 150 kHz lie between 1.4 cm and 4.2 cm. The upper reinforcement bars are 7.5cm underneath the top surface and the artificial crack is $17.5cm$ away from the nearest side surface (see Fig. 5.2). Interferences on Rayleigh wave measurements due to the discontinuities do not occur.

5.2 Specimen 2

Figure 5.3: Concrete specimen for surface-breaking crack charaterization.

The specimen for the surface-breaking notch measurement is cast from ASTM C 150 Type I portland cement, natural sand and coarse, crushed granitic gneiss aggregate with a water to cement ratio of 0.45 by mass. The dimensions in width, length are 33 x 60.96 x 25.4 cm, respectively. After mixing the components, the concrete is placed in wooden molds (30.48 x 40.64 x 68.58 cm). After the initial setting time, the concrete is covered with plastic sheeting. It is cured for 24h before the molds are stripped and the specimens are placed in a controlled environment nominally of 23C and 95% relative humidity for 28 days after the curing period. Until the measurements are conducted the specimen is stored in a laboratory environment [16]. More information about the composition of the specimen can be found in Table 5.2, 5.3 and 5.4.

Table 5.2: Gradation of fine aggregate [10, 16].

Sieve size	Amount retained/ total weight (%)
#4	6.2
#8	7.1
#16	14.8
#30	18.7
#50	33.0
#100	15.8
Pan	4.4
Total	100

Table 5.3: Gradation of coarse aggregate [10, 16].

Sieve size	Amount retained/ total weight (%)
$1/2''$	33.3
$3/8''$	33.3
#4	33.3

Table 5.4: Mix design for concrete sample [10, 16].

Coarse aggregate	1890 ($\frac{lb}{yd^3}$)
Fine aggregate	1130 ($\frac{lb}{yd^3}$)
Cement	720 ($\frac{lb}{yd^3}$)
Water	324 ($\frac{lb}{yd^3}$)

CHAPTER VI

ATTENUATION AND PHASE VELOCITY MEASUREMENT

Attenuation and phase veloity are crucial parameters for the assessment of the durability of concrete as already mentioned in the introduction. Important conclusions about the condition of the material can be drawn as Punurai et al. and Soltani et al. have shown in [8, 27]. The attenuation coefficient of Rayleigh surface waves can be determined experimentally by the spectral ratio analysis. This procedure has also been applied by Punurai et al. in [27] and by In et al. in [6]. The following processing of the data will be done according to the work about attenuation and phase velocity in these papers.

6.1 Rayleigh wave generation and Data acquisition

The goal is to be able to generate the Rayleigh surface wave with a setup that can be used for in-field measurements. Those in-field concrete structures have rough surfaces and one would have to polish the desired points of inspections to be able to take measurements with the contact ultrasonic setup. This is very impractical. To address this issue and overcome the drawbacks the Rayleigh surface wave is generated in the material with the introduced non contact setup. The transducers are inclined at the critical angle to generate and detect Rayleigh surface waves in the specimen. The critical angle is calculated with Snell's Law:

$$\theta_{cr} = sin^{-1}\frac{c_L}{c_R}, \tag{73}$$

where c_L is the velocity of the pressure wave in air emitted by the transmitter and c_R is the Rayleigh wave velocity in the specimen. The time signal of the generated Rayleigh wave is obtained by a second air-coupled transducer which is also inclined at the same critical angle. The setup is run in a pitch-catch mode with two transducers. The sampling rate of the signals is $5MHz$ which means the $1ms$ long signal consists of 5000 measurement points. Two measurements over propagation distances of $17.8cm$ and $25.4cm$ are made. Figure 6.1 displays the measured time signals of the Rayleigh waves.

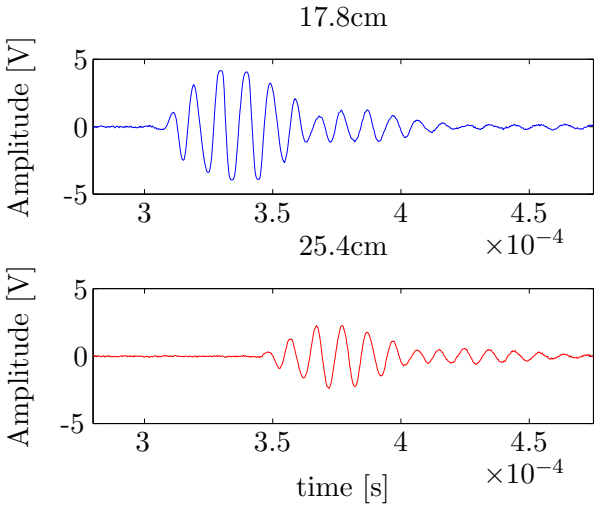

Figure 6.1: Two measured wave signals for the different distances z_1 and z_2.

The decrease in the amplitude of the wave detected at the longer distance is clearly seen. This decay in the amplitude will be used to calculate the attenutation of the Rayleigh wave in the specimen. Also the arrival time difference for the different distances is apparent.

6.2 Data analysis

To calculate the attenuation and phase velocity one cycle of the Rayleigh wave signal is extracted from the whole measured signal. The reason for taking only one cycle out of the signals is that these transducers are narrow band transducer such that at the the first cycle, which is a broadband pulse, the transducers behaviour at its resonance frequency is dominant in the generated signal. A Hann window is then applied over the extraced cycle of the signal.

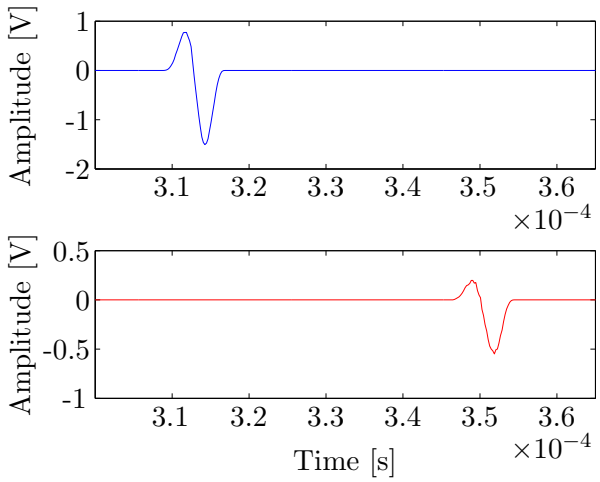

Figure 6.2: Signal after Hann window is applied.

Subsequently a Fast Fourier Transformation is performed to obtain the amplitude spectrum. With the procedure shown in 3.2.1 we can now calculate the attenuation and phase velocity.

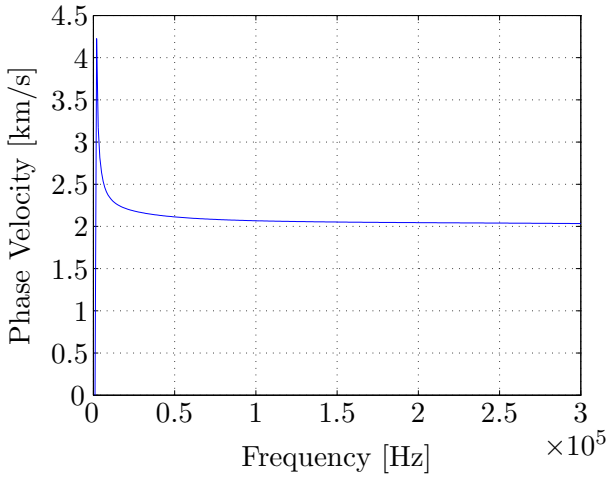

Figure 6.3: Phase velocity of the Rayleigh wave.

Fig. 6.3 shows the calculated phase velocity between $0kHz$ and $300kHz$. The velocity has a slightly negative slope in the considered frequency range between $50kHz$ and $150kHz$ which results from the nonhomogenous material of the concrete specimen. The wave is, therefore, weakly dispersive.

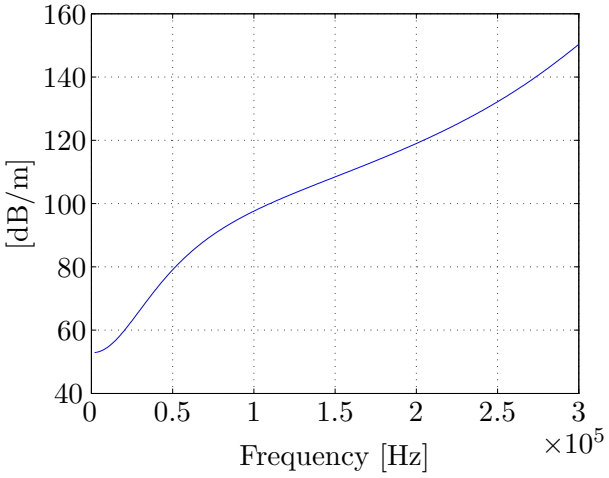

Figure 6.4: Attenuation coefficient for a Rayleigh wave propagating over a distance of $7.6cm$.

The attenuation value is reasonable for this kind of concrete. The non-monotonic slope can be explained by the earlier mentioned scattering effect which has a different contribution on the attenuation for different frequency regions. With the earlier estimated averaged size of the aggregates and the measured Rayleigh wave velocity of $2100m/s$ the scattering regime can be determined with the definitions in 3.2. Whereupon the stochastic regime, where the attenuation is a function of the frequency square, starts between $42kHz$ and $67kHz$. A transition towards a quadratic progression of the attenuation can be seen in this region in Fig. 6.4. However, an exact determinaton where the the different regimes start is very difficult to say because of the inhomogenity of the specimen which leads to slightly different shapes of the attenuation for measurements at different spots. Fig. 6.5 shows the result of a second attenuation measurement over a distance of $5.1cm$.

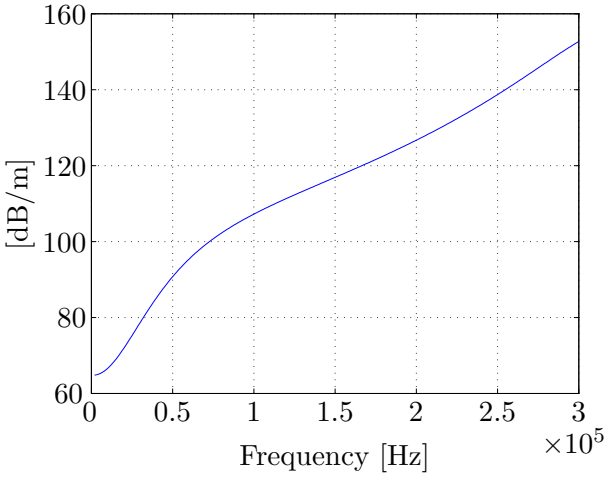

Figure 6.5: Attenuation coefficient for a Rayleigh wave propagating over a distance of $5.1cm$.

Again the quadratic progression can be seen for higher frequencies, however, it is difficult to determine a narrow frequency window in which the change from the rayleigh to the stochastic regime happens.

CHAPTER VII

IMAGING OF ARTIFICIAL CRACK AND REINFORCEMENT BAR

Being able to detect cracks that originate underneath the surface is especially important because by the time they can be seen at the surface they depict already a major risk to the structure. It is therefore important to detect those cracks in an early stage in order to be able to take a maintenance action. Also the monitoring of the rebars is of great importance to ensure the stability of concrete structures. The imaging of the artificial crack and the reinforcement bar is done in the pitch catch mode. The pulse echo method, and thereofore only one transducer, would reduce the propagation distance of the signal and therefore the signal would lose less energy between transmitting and receiving. However, the reflection from the surface of the specimen after the signal gets emitted from the transducer would be too strong and the signal coming from the reflection of the discontinuity could not be detected in a reliable manner. Therefore, two transducers are used in a pitch-catch mode, one for transmitting and teh other one for receiving. In this experiment it is also very interesting to see if the longitudinal wave that is generated in the specimen has enough energy to propagate to the crack and if there is still a sufficiently strong signal that arrives at the receiver. The imaging of the reinforcement bars will give conclusions about how exact the imaging is and how sensitive the setup is in receiving signals since the diameter of the reinforcement bars is only $2.5cm$, relatively small and only a fraction of the signal in the specimen will be reflected back to the receiving transducer.

7.1 Phase velocity in air

To be able to detect the discontinuities it is important to be able to distinguish signals originating from reflections on the discontinuities from other signals. This can be done by calculating the expected arrival time of the signal. All other signals that are not detected at this time can be neglected. It is therefore important to not only know the phase velocity of the wave propagating in the specimen but also the phase velocity in air under laboratory

conditions. To measure the phase velocity in air two transducers are aligned facing each other on two aluminum rods as shown in Fig. 7.1.

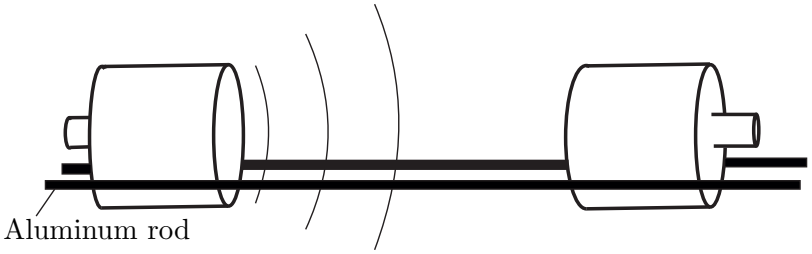

Figure 7.1: Setup of the transducers for the measurement.

Two measurements over two different distances are made. These two time signals are processed as shown in 3.2.1 to calculate the phase velocity. The diffraction, however, is corrected with the diffraction correction for longitudinal ultrsound proposed by Rogers and van Buren (Eq. 60 in chapter 3.2) Fig. 7.2 shows the result of the calculation.

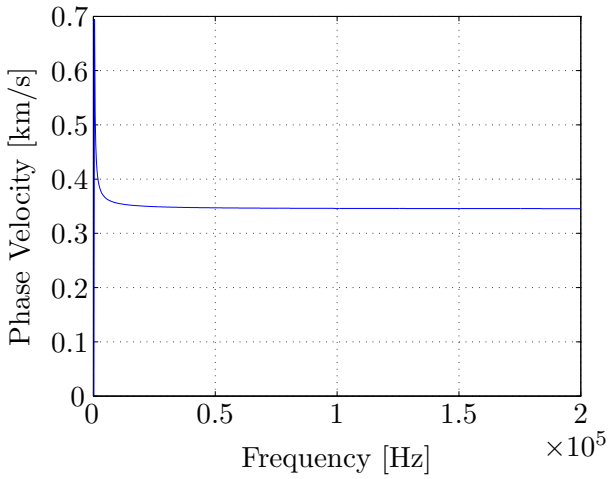

Figure 7.2: Phase velocity in air.

The phase velocity in air in the laboratory is $345m/s$ for the relevant frequency range around $100kHz$.

7.2 Generation of longitudinal wave

The transducers need to be oriented at the appropriate angle to be able to detect the discontinuites. The idea is to generate a longitudinal wave that propagates through the

specimen and gets reflected by the discontinuity. The reflected signal is then detected by the receiving transducer.

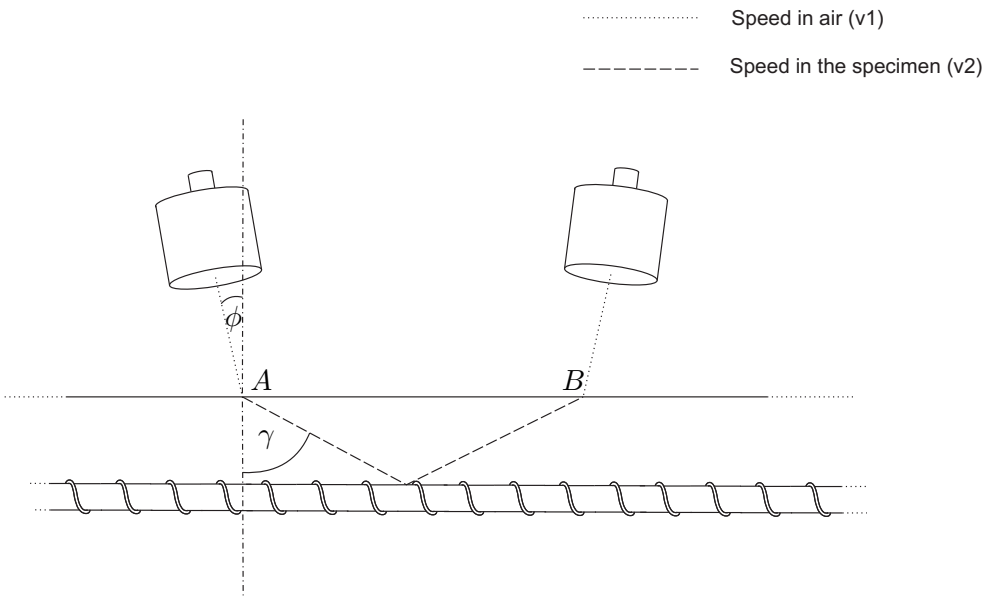

Figure 7.3: Detection of discotinuities in the concrete sample.

This refraction angle is determined by Snell's law.

$$\frac{sin(\phi)}{v_1} = \frac{sin(\gamma)}{v_2}. \tag{74}$$

The wave speed of a longitudinal wave is $3770m/s$ and is calculated by measuring the time-of-flight of a longitudinal wave traveling through one width of the concrete specimen [7].

7.3 Crack

The artificial crack extends over one half of the profile of the specimen. The measurements to detect the crack were performed after flipping specimen 1 upside down so that the propagating waves wouldn't get influenced by the rebars. This was done because the reinforcement bars caused to much reflections and it was not possible to filter out the reflections that originated from the crack. This way the crack is $17.5cm$ underneath the suface. For the measurement the transducers were moved together as closely as possible to still be able to place a barrier for the acoustic signal in between the transducers. The distance between

the center of the transducers was $15.25cm$. Putting the transducers closer together reduces the distance which the wave has to propagate from the transmitter to the crack and back to receiver. The signal loses less energy on a shorter distance and a stronger signal from the refelection can be detected. The orientation of the transducers is calculated with Snell's law. From the distance between the transducers ($15.25cm$), the distance of the crack to the surface ($15.25cm$), the speed of the ultrasound in the air ($345\frac{m}{s}$) and the wave speed in the specimen ($3770\frac{m}{s}$) the angle can be calculated:

$$\phi = sin^{-1} \cdot \left(345\frac{m}{s} \cdot \frac{sin(tan^{-1}(\frac{7.63}{17.5}))}{3770\frac{m}{s}} \right) = 2.096\,^{\circ} \tag{75}$$

This calculation is done under the assumption that ϕ is small and the distance of $15.25cm$ between the transducer can also be assumed to be approximately the distance between point A and B in Fig. 7.3. Making this assumption leads in the calculation to a angle ϕ that is slightly too big, which should be considered in the experiment.

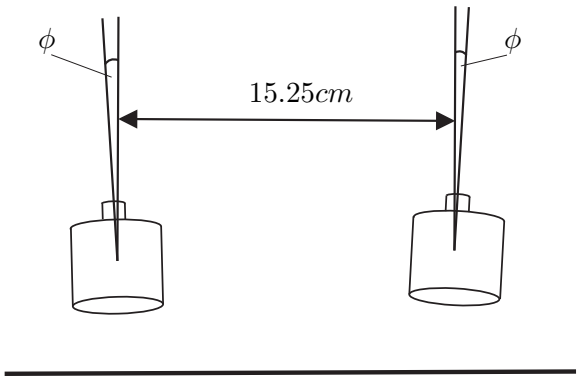

Figure 7.4: Arrangement of the transducers for the crack detection.

Orienting the transducers in this angle makes it possible to detect the reflection of the longitudinal wave from the crack. By knowing the propagation distance and the velocities of the ultrasound in air and in the specimen it is also possible to estimate a time frame in which the reflected signal should be detected. The transducers were lifted off $3.5cm$ from the surface and the propagation distance can be calculated to be approximatley $38.2cm$.

The expected arrival time is then calculated to be

$$\frac{0.382m}{3770\frac{m}{s}} + \frac{0.07m}{345\frac{m}{s}} = 0.304 \cdot 10^{-3}s. \tag{76}$$

This is very helpful to see if the results are reasonable. However, the actual gate in which the data were evaluated was determined after the measurement. Exemplary wave signals from measurements on the sample next to the crack and over the crack are shown in Fig. 7.5 and Fig. 7.6.

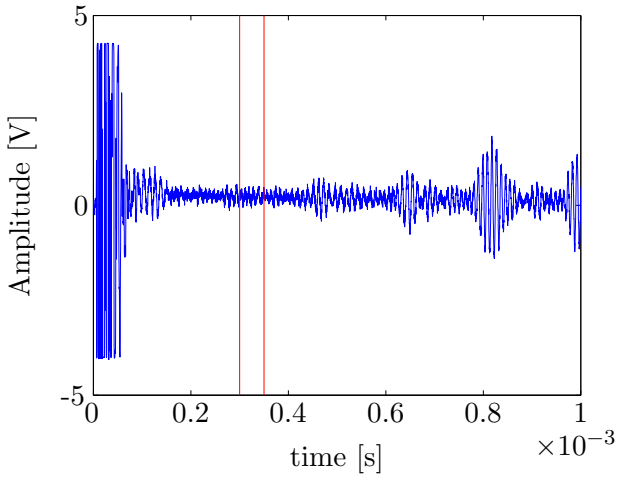

Figure 7.5: Time signal from measurement in the area without the crack.

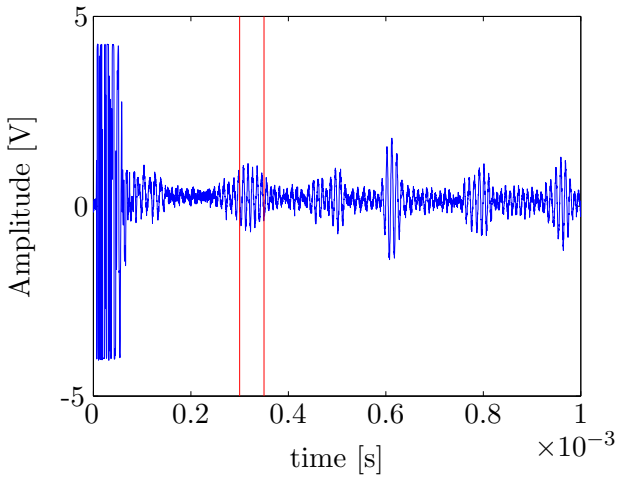

Figure 7.6: Time signal of the reflected wave over the crack.

At around the estimated time an amplitude can be seen in the time signals that are obtained from measurements over the crack. This amplitude is due to the refelction of the

longitudinal wave at the crack. After obtaining the data the gate for the evaluation and postprocessing was set between $0.3 \cdot 10^{-3}s$ and $0.35 \cdot 10^{-3}s$. This time frame was used for all the time signals that were obtained through the measurement. The highest amplitude in the gate was compared to the amplitude of the noise. The factor by which the amplitude in the gate was higher than the noise is indicated with different colors in the scale in Fig. 7.7. Fig. 7.7 shows all the points at which measurements were taken. The points are colored according to the strength of the reflection of the signal from the crack.

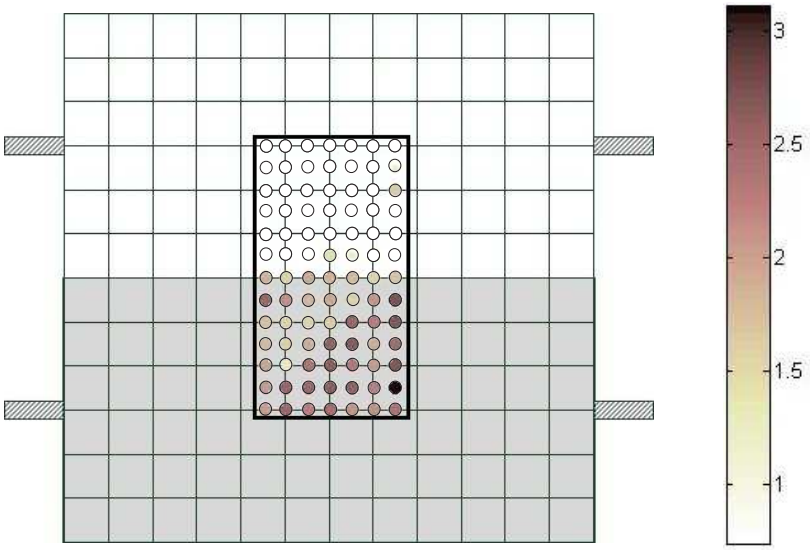

Figure 7.7: Crack detection in the area of the black box. The lower grey half represents the area over the crack.

Good agreement exists between the measurement and the actual location of the crack.

7.4 Reinforcement Bar

Besides the crack there are also four rebars in this concrete specimen. They are embadded in the specimen at two different heights. Always two of the four are arranged parallel at the same height. The first pair of rebars is $7.5cm$ from the surface and the second pair is at a distance of $10.8cm$ from the surface. In this experiment the goal is to detect the two upper rebars. The reinforcement bars have a diameter of $2.5cm$ and are made of steel. This is relativley small for the detection with $100kHz$ ultrasound and the transducers with a diameter of $5cm$ that are used for the measurements. The fact that the rebars are not

smooth but have a surface texture makes the detection through reflection of the ultrasonic wave even more difficult. To increase the smooth reflection area the transducers are a little further apart from each other compared to the measurement of the crack. $20.32cm$ is the distance in this case. This leads to a bigger inclination of the transducers and are shallower angle in which the wave will hit the rebar. With the bigger reflection area the ratio between smooth reflection areas and bumps from the texture improves. The inclination angle is then calculted in the same way as it was for the detection of the crack.

$$\phi = sin^{-1} \cdot \left(345\frac{m}{s} \cdot \frac{sin(tan^{-1}(\frac{10.16cm}{7.5}))}{3770\frac{m}{s}} \right) = 4.222\,^{\circ} \tag{77}$$

Again the calculation of the incident angle for the crack detection is done under the assumption that the distance between the points A and B in Fig. 7.3 is equal to the distance between the transducers. In this case the actual angle with which the discontinuity can be detected is slighly smaller, as well.

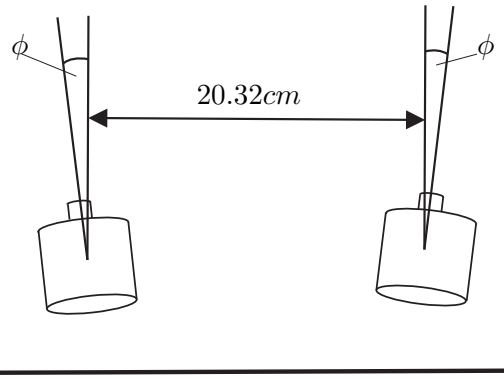

Figure 7.8: Arrangement of the transducers for the rebar detection.

The transducers were lifted off $3.5cm$ from the surface and the propagation distance is $25.3cm$ in this case. The expected arrival time is then calculated to

$$\frac{0.253m}{3770\frac{m}{s}} + \frac{0.07m}{345\frac{m}{s}} = 0.27 \cdot 10^{-3}s. \tag{78}$$

The procedure of the evaluation of the data is equivalent to the procedure of the crack detection. Again time signals are shown in Fig. 7.9 and Fig. 7.10 exemplary for measurements next to and over the rebars.

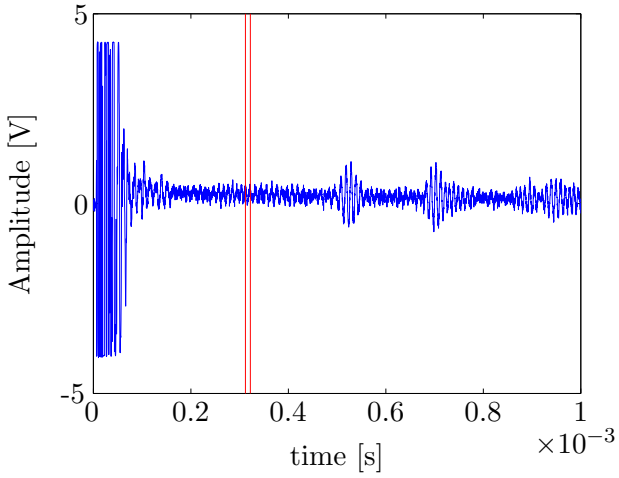

Figure 7.9: Time signal of the wave for the rebar detection.

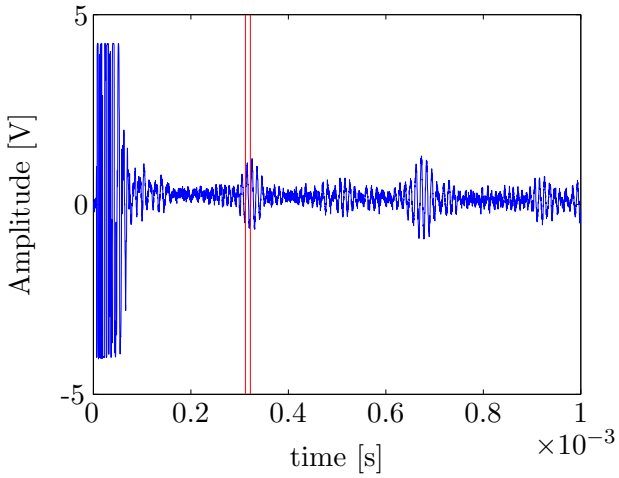

Figure 7.10: Time signal of the wave for the rebar detection.

Again it can be seen that the reflection occurs in the approximately calculated time. Also in this case, the gate in which the time signals were evaluated is adjusted after the measurement is performed. The earlier calculation of the arrival time is just an approximate indication of when the reflected signal should be expected but cannot serve as an exact determination for the time frame for evaluating the data. Fig. 7.11 shows the result after the data processing.

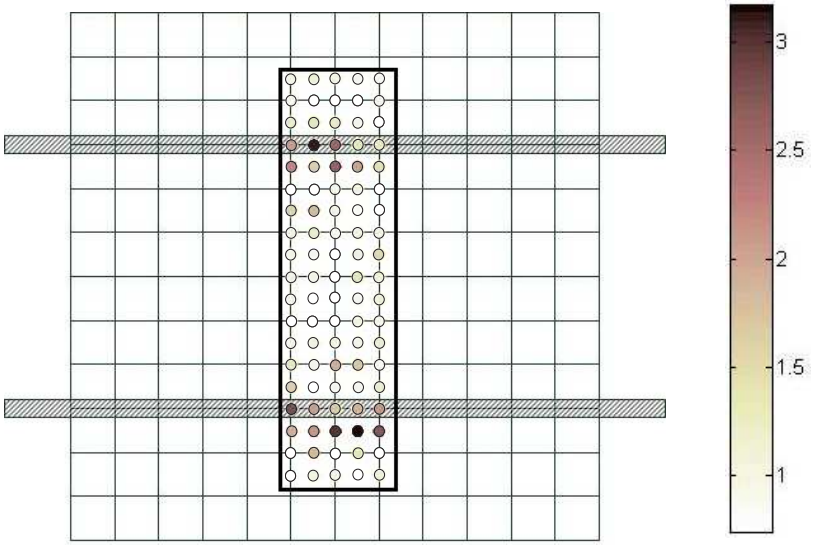

Figure 7.11: Bar.

The result is not as accurate as the result of the crack detection. However, the two rebars and their position can be recognized in this image. The diameter of the rebars which is smaller than the wavelength ($\lambda = 3.8cm$; $diameter = 2.5cm$) makes it hard to get a nice reflected signal for all the measurements that were taken in the area over the rebars.

CHAPTER VIII

SURFACE-BREAKING NOTCH

Major damage of concrete structures evolve from small cracks in surfaces. This small cracks can rapidly grow and become a risk for the durability of the structure. Those surface cracks could also expose reinforcement bars that are embedded in the concrete to the surroundings, which could lead to corrosion. It is therefore important to monitor those surface-breaking cracks and to know how deep the crack has penerated into the specimen. A lot of work has been done on characterizing surface-breaking cracks with surface waves in concrete experimentally [4, 5, 11–14, 24, 25] and with numerical models [3, 9, 28]. However, a non-contact generation of surface waves with air-coupled transducer hasn't been accomplished. This has advantages over the impact-echo technique which is used in [13, 14]. Due to the electronically generated signals, the output signals are almost exactly the same given the experimental setup. The measured signals can, therfore, be averaged in a short time in contrast to mechanically generated signals where averaging is difficult. In this experiment measurements are performed on a notch that simulates a crack. Angel and Achenbach proposed an analytical solution in [3] with which the crack depth can be obtained from the transmission coefficient of Rayleigh waves propagating across the crack. Song et al. created a model to calculate the surface wave transmission coefficient at a notch with the boundary element method. In the model a normally incident surface wave on the notch is generated by a impact source [28]. The analytical solution of Angel and Achenbach and the result of Song et al. model are displayed in Fig. 8.1.

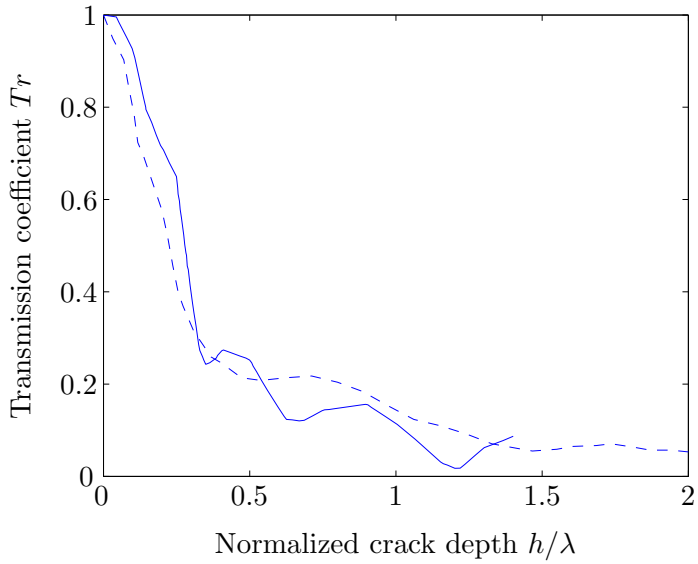

Figure 8.1: The transmission coefficient is plotted versus the crack depth normalized with the wavelength of the incident wave. The solid line is the analytical solution of Angel and Achenbach for transmission coefficient of Rayleigh waves, across the crack of depth h. The dashed line is the result of the model of Song et al.

The transmission coefficient is the amplitude of the transmitted wave normalized by that of the incident wave. This relationship between transmission coefficient and normalized crack depth from Angel and Achenbach is for a Poisson's ratio of 0.3. Song et al. used a Poisson's ratio of 0.289 in the numerical model. For normalized crack depth greater than 0.4 the Poisson's ratio has an influence and this has to be considered in interpreting the results. In the experiment that is described in this chapter the fully non contact ultrasonic setup is used to measure the transmission coefficient of Rayleigh surface waves and then the notch depth is estimated using the relationship between the transmission coefficient Tr and the normalized notch depth h/λ.

8.1 Notch preperation

Since the concrete sample was not casted for the purpose of this measurements the notch had to be sawn into the already cured specimen. The notch was made with a Dremel rotary tool. The width of the notch is defined by the thickness of the cutting wheel on the rotary device. The thickness of the diamond cutting wheel that was used for this notch is $0.6mm$.

Measurements are performed up to a value for h/λ of 0.3.

8.2 Experimental setup

The experimental setup is compared to the setups in the previous experiments modified on the transmitting side. The pulse reveicer is peplaced by a function generator and an amplifier as shown in Figure 4.1. This is done to be able to generate signals at different frequencies and do a frequency sweep to get multiple data points instead of changing the crack depth for every single measurement. The frequency range for this measurement was between $80kHz$ and $140kHz$. However, the spectral ratio analysis showed that the actual frequency of the measured signal might differ from the initial sinusoidal signal generated by the function generator. This issue will be explained in more detail later in this chapter.
This setup has a great advantage over the impact-echo method since Rayleigh surface waved are directly generated what makes the data processing after the measurements much easier. The impact-echo method generates multiple waves in the specimen and the Rayleigh wave has to be extracted from the measured time domain signal.

8.3 Phase velocity measurement

Since the crack depth is normalized with the wavelength, we need to know the exact Rayleigh wave velocity in specimen 2. To calculate the critical angle the velocity is estimated to be roughly $2000m/s$. After orientating the transuducer the angle is optimized to the point where the amplitude of the signal in the oscilloscope is maximal. Subsequently two measurements over two different distances are made and the data is processed as desrcibed in chapter 6.1 to obtain the phase velocity. The Rayleigh wave phase velocity over the frequency is shown in Fig. 8.2.

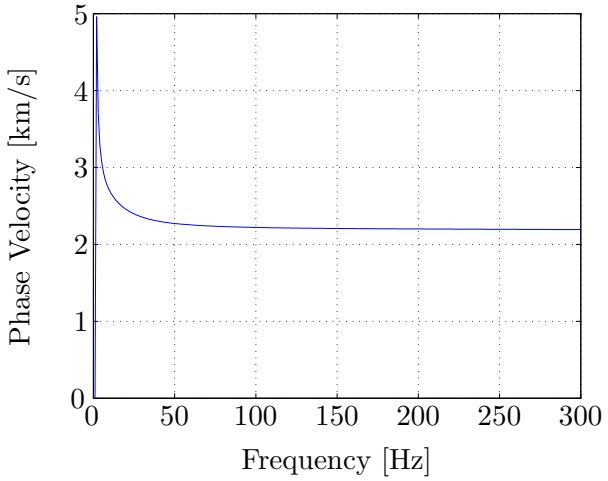

Figure 8.2: Phase velocity of the Rayleigh wave in specimen 2.

The phase velocity is in the frequncy range of interest for the $100kHz$ transducer around $2200m/s$. The exact values of the phase velocity at the different frequencies is used for the wavelength calculation.

8.4 Transmission coefficient measurement

The first measurements are performed with the $100kHz$ transducer inclined at the Rayleigh wave critical angle and placed at a distance of $12.7cm$ from the crack (cf. Fig. 8.3). This is in ther far field according to Cheng and Achenbach who suggested that a distance $x = 5\lambda$ can be considered as far field [5]. Near field effects in the vicinity of the crack have, therfore, no impact on the measurement. The notch has a depth of $h = 0.5cm$.

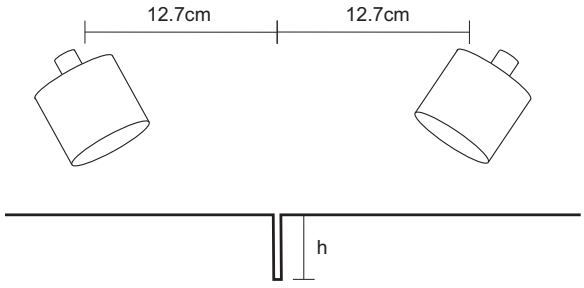

Figure 8.3: Measurement setup.

The function generator generates a sinusoidal signal with frequencies from $80kHz$ to $140kHz$. Measurements are taken in $2kHz$ intervals between these two frequencies. The

Rayleigh wave is then extracted from the measured signal in the following data processing and a Hann window is applied. Fig. 8.4 shows the Rayleigh wave signal before and after the Hann window is applied.

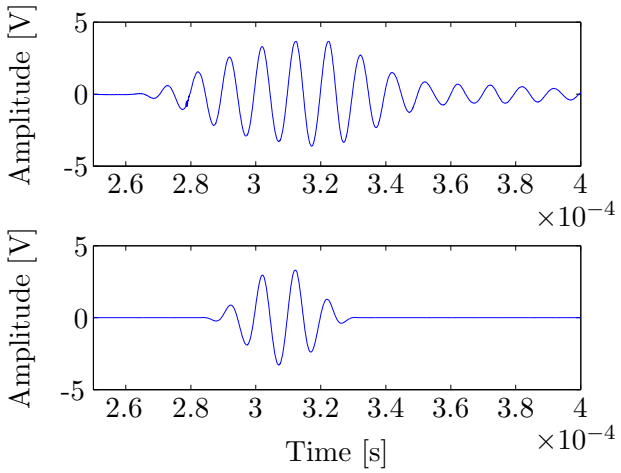

Figure 8.4: Rayleigh wave signal (above) and signal after Hann window is applied (below).

Subsequently an FFT is performed. The same procedure was done on the signal obtained from a crack free region to normalize the data.

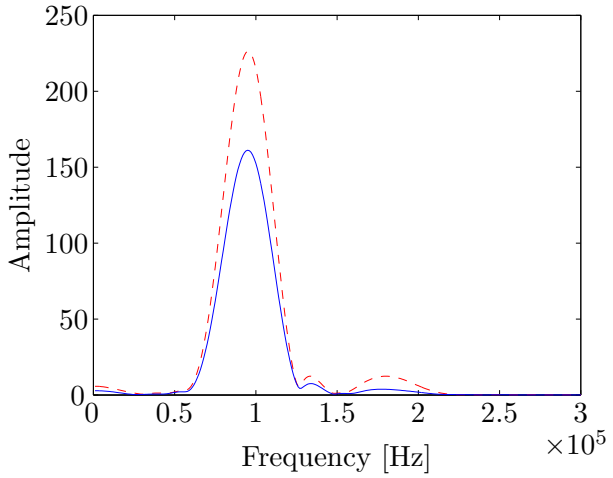

Figure 8.5: Frequency spectrum of signal after propagating over the crack (solid blue) and from crack free model measurements (dashed red).

The transmission coefficient is now obtained by dividing the maximum value of the frequency spectrum from the measurement on the specimen with the crack by the maximum value of the frequency spectrum from the measurement on the crack-free specimen. Before

doing so it is checked that the peaks of both spectra are at the same frequency. A Rayleigh wave that was generated by a sinusoidal signal with a certain frequency from the function generator has, after performing a FFT, not necessarily its peak at the very frequency that the initial input signal had. All signals need, therefore, to be checked for the frequency at the maximum value of their frequency spectrum before calculating the transmission coefficient. This issue leads also to a loss of some measurement points since frequencies are shifted and no matching frequency from either the model with crack or the one without crack can be found.

8.5 Results

For one setup, two sets of measurements were conducted. After finishing one measurement the transmitter and receiver are switched: the transmitting transducer is reconnected to be the receiving transducer and the receiving transducer is switched to become the transmitting transducer (the circles and the diamonds in Fig. 8.6 and Fig. 8.7 distinguish the results from the different measurement sets). The result measured with a crack depth of $0.5cm$ and a frequency swept from $80kHz$ to $140kHz$ are shown in Fig. 8.6. For this results 6 cycles of the Rayleigh wave are taken out of the time signal for the data processing.

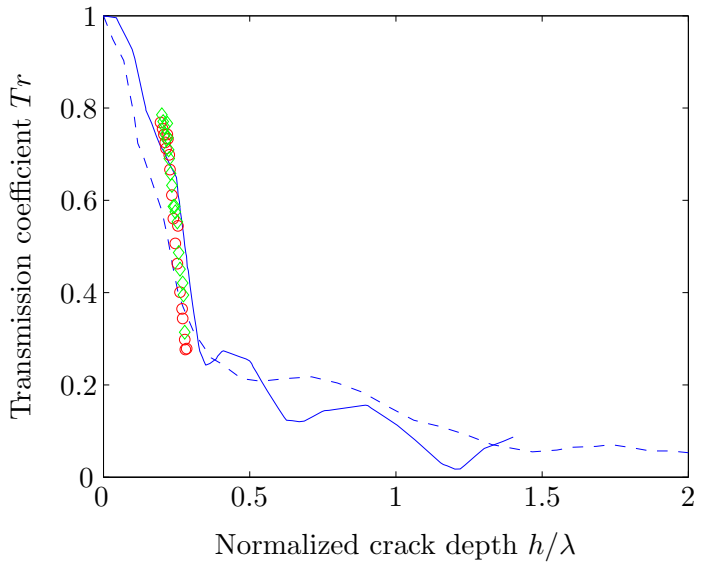

Figure 8.6: Transmission coefficient calculated by taking six cycles of the measured Rayleigh wave.

The actual frequency range of the data points for the circles is between $87kHz$ and $126kHz$ which means a normalized crack depth from $\frac{h}{\lambda} = 0.2$ to $\frac{h}{\lambda} = 0.29$. The diamond data points have frequencies between $89kHz$ and $123kHz$. The data points lie between a normalized crack depth of $\frac{h}{\lambda} = 0.2$ and $\frac{h}{\lambda} = 0.28$. The loss of data points is due to the earlier described issue that the frequencies of the generated sinusoidal signal are not equal to the frequency where the maximum amplitude is located after the FFT is performed and the signals evaluated. Taking a different signal lengths of the Rayleigh wave for the data processing leads to slightly different results. In Fig. 8.7 only five cycles are taken from the Rayleigh wave signal for the further data processing.

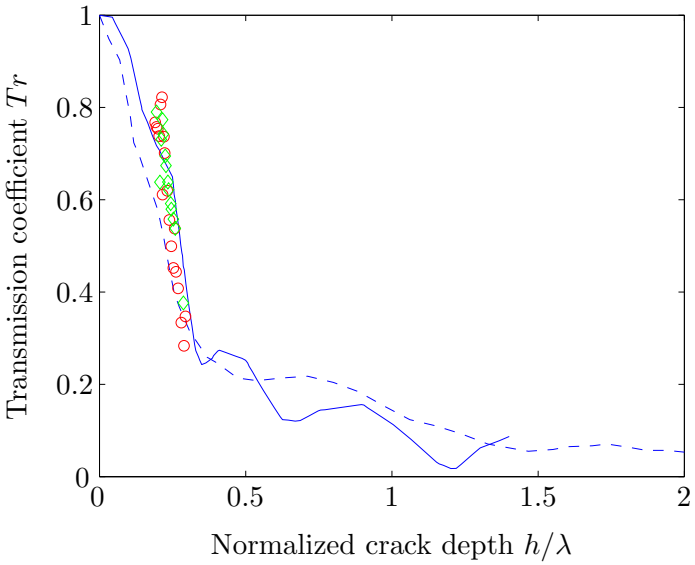

Figure 8.7: Transmission coefficient calculated by taking five cycles of the measured Rayleigh wave.

In this case the frequency range lies between $85kHz$ and $130kHz$ for the circle data points. The normalized crack depth is between $\frac{h}{\lambda} = 0.19$ and $\frac{h}{\lambda} = 0.29$. For the diamonds the frequency range is between $87kHz$ and $127kHz$ and the normalized crack depth between $\frac{h}{\lambda} = 0.2$ and $\frac{h}{\lambda} = 0.29$. The results lie in the range of the analytical solution from Angel and Achenbach and the prediction of Song et al.'s model. In both figures the data points from the measurement are closer to the solution from Angel and Achenbach. Neither of the analytical solutions can be considered to be exact, especially not for the characteristics

of this notch in the specimen and this experimental setup in generally. Both analytical solutions, however, help to see whether or not the obtained results are in a reasonable range. Both, Figure 8.7 and Figure 8.6 with the results show that this is the case. A depth measurement of simulated cracks, like the notch in this experiment, seems, therefore, to be feasible with the non-contact air-coupled measurement setup.

CHAPTER IX

CONCLUSION AND FUTURE WORK

9.1 Conclusion

The fully noncontact air-coupled measurement setup that is introduced in this thesis is highly promising. Despite the high impedance mismatch between air and the concrete specimen the setup can generate strong enough signals with an appropriate preamplification, a signal to noise ratio of $30dB$ can be achieved; this is sufficient for the analysis of waveforms and imaging. Rayleigh wave attenuation and phase velocity measurements are possible with this setup. Also deep penetration with air-coupled generated longitudinal waves (e.g. 7.5 cm for the imaging of the upper rebars and 17.5 cm for the crack) is possible to detect discontinuities in concrete structure. Due to the fully noncontact setup it is possible to make rapid scanning and fast measurement since surface preparation is not necessary. The surface-breaking crack measurements show good agreement with a theoretical solution proposed by Angel and Achenbach in [3] and the solution from the numerical model created by Song et al.. The handling of the setup is very easy and, as compared to the conventional contact ultrasonic setup, is close to an application for in-field use to test concrete structures. The direct generation of Rayleigh waves is a great advantage over the impact-echo method, by which also many other waves are generated, and makes the data processing much easier. Also the electronically generated output signals are almost identical for every measurement which makes a fast averaging of many measured signals possible, whereas, for mechanically generated signals this is not as easy.

9.2 Future Work

In future work also the attenuation measurements from this intact concrete samples may be compared to data obtained from damaged concrete. It has been shown in this thesis that attenuation and phase velocity measurements are feasable with this setup. The actual comparison with damaged concrete is still to be done. Also for the imaging of discontinuities

improvements can be made. The incident angle of the ultrasonic waves are very important for the propagating wave in the specimen to actually hit the discontinuity and also to detect the reflection. Skewed surfaces will lead to different incident angles at which the ultrasonic waves hit the specimen. To detect, for example, reinforcement bars, an exact inclination of the transducers is necessary to be able to receive a reflection signal. Changing incident angle is therefore not recommended. If the mounting of the transducers would, therefore, be in such a way that the transducers can follow conformally to the curved or uneven surface during the scanning over the surface respectable imrpovements could be accomplished.

References

[1] Achenbach, J. D., *Wave Propagation in Elastic Solids*, vol. 16 of *Applied Mathematics and Mechanics*. Amsterdam . London: North-Holland Publishing Company, 1973.

[2] AggregateIndustries *http://www.aggregate-us.com*.

[3] Angel, Y. C. and Achenbach, J. D., "Reflection and transmission of obliquely incident rayleigh waves by a surface-breaking crack," *Journal of the Acoustical Society of America*, vol. 75, pp. 313–319, Feb. 1984.

[4] C. H. Yew, K. C. and Wang, D. L., "A experimental study of interaction betwen surface waves and a surface breaking crack," *J. Acoust. Soc. Am.*, vol. 75, pp. 189–196, Jan. 1984.

[5] Cheng, A. and Achenbach, J. D., "A roller device scan for surface-breaking cracks and to determine crack depth by self-calibrating ultrasonic technique," *Research in Nondestructive Evaluation*, vol. 7, pp. 185–194, 1996.

[6] Chi-Won In, e. a., "Characterization of ultrasonic rayleigh surface waves in asphaltic concrete," *Elsevier NDT&E International*, vol. 42, pp. 610–617, May 2009.

[7] Dolphyn, B., "Post-tensioned containment mock-up and tendon monitoring program," *Second-Year Report for the Electric Power Research Institute; Georgia Institute of Technology*, Dec. 2012.

[8] Fethi Soltani, e. a., "Relationship between ultrasonic rayleigh wave propagation and capillary porosity in cement paste with variable water content," *Elsevier. NDT&E International*, vol. 54, pp. 75–83, Mar. 2013.

[9] G. Hevin, e. a., "Characterisation of surface cracks with rayleigh waves: a numerical model," *NDT&E International*, vol. 31, no. 4, pp. 289–297, 1998.

[10] In, C.-W., *Defect Characterization in Heterogeneous Civil Materials Using Ultrasound*. PhD dissertation, Georgia Institute of Technology, School of Civil and Environmental Engineering, May 2013.

[11] J. D. Achenbach, e. a., "Self-calibrating ultrasonic technique for crack depth measurement," *Journal of Nondestructive Evaluation*, vol. 11, no. 2, pp. 103–108, 1992.

[12] John S Popovics, e. a., "Application of surface wave transmission measurements for crack depth determination in concrete," *ACI Materials Journal*, vol. 97, no. 2, pp. 127–139, 2000.

[13] Kee, S.-H. and Zhu, J., "Using air-coupled sensors to determine the depth of a surface-breaking crack in concrete.," *Journal of the Acoustical Society of America*, vol. 127, pp. 1279–1287, Mar. 2010.

[14] Kee, S.-H. and Zhu, J., "Effects of sensor locations on air-coupled surface wave transmission measurements across a surface-breking crack.," *IEEE*, vol. 58, pp. 427–436, Feb. 2011.

[15] M. Castaings, e. a., "Single sided inspection of composite materials using air coupled ultrasound.," *Journal of Nondestructive Evaluation*, vol. 17, no. 1, pp. 37–45, 1998.

[16] Matthias Seher, e. a., "Numerical and experimental study of crack depth measurement in concrete using diffuse ultrasound," *Journal of Nondestructive Evaluation*, vol. 32, pp. 81–92, 2013.

[17] Owino, J. O. and Laurence J. Jacobs, Member, A., "Attenuation measurement in cement-based materials using laser ultrasonics," *Journal of Engineering Mechanics*, vol. 125, no. 6, pp. 637–647, 1999.

[18] Punurai, W., *Cement-based Materials' Characterization using Ultrasonic Attenuation*. PhD dissertation, Georgia Institute of Technology, School of Civil and Environmental Engineering, May 2006.

[19] Rogers, P. H. and Buren, A. L. V., "An exact expression for the lommel diffraction correction integral," *Journal of the Acoustical Society of America*, vol. 55, pp. 724–728, Jan. 1974.

[20] Rose, J. L. and Nagy, P. B., "Ultrasonic waves in solid media," *Journal of the Acoustical Society of America*, vol. 107, no. 4, pp. 1807–1808, 2000.

[21] Ruiz, A. and Nagy, P. B., "Diffraction correction for precision surface aoustic wave velocity measurements," *Journal of the Acoustical Society of America*, vol. 112, pp. 835–842, Sept. 2002.

[22] Sachse, W. and Pao, Y.-H., "On the determination of phase and group velocities of dispersive wave in solids," *Journal of Applied Physics*, vol. 49, pp. 4320–4327, Aug. 1978.

[23] Stoessel, R., *Air-Coupled Ultrasound Inspection as a New Non-Destrucive Testing Tool for Quality Assuarance*. PhD dissertation, Universitaet Stuttgart, Institut fuer Kunstoffpruefung und Kunststoffkunde, 2004.

[24] Sung Woo Shin, e. a., "Crack depth estimation in concrete using energy transmission of surface waves," *ACI Materials Journal*, vol. 105, no. 5, pp. 510–516, 2008.

[25] Viktorov, I. A., *Rayleigh and Lamb Waves Physical Theory and Applications*. Plenum Press New York, 1967.

[26] Vincent Garnier, e. a., "Acoustic techniques for concrete evaluation: Improvements comparisons and consistency.," *Elsevier Construction and Building Materials*, vol. 43, pp. 598–613, 2013.

[27] Wonsiri Punurai, e. a., "Characterization of entrained air voids in cement paste with scattered ultrasound," *NDT&E International*, vol. 39, pp. 514–524, 2006.

[28] Woon-Joon Song, e. a., "Measurement of surface wave transmission coefficient across surface-breaking cracks and notches in concrete," *Journal of the Acoustical Society of America*, vol. 113, pp. 717–725, Feb. 2003.